THERMOPOWER OF TANTALUM DISELENIDE IN THE CHARGE DENSITY WAVE REGIME

by

Sabaratnasingam Gnanarajan

B.Sc.(hon.) University of Jaffna, Jaffna, Sri Lanka, 1981

THESIS SUBMITTED IN PARTIAL FULFILLMENT OF

THE REQUIREMENTS FOR THE DEGREE OF

MASTER OF SCIENCE

in the Department

of

Physics

© Sabaratnasingam Gnanarajan 1985

SIMON FRASER UNIVERSITY

May, 1984

All rights reserved. This work may not be reproduced in whole or in part, by photocopy or other means, without permission of the author.

APPROVAL

Name: Sabaratnasingam Gnanarajan

Degree: Master of Science

Title of thesis: Thermopower of Tantalum Diselenide in the charge density wave Regime

Examining Committee:

Chairperson: J. C. Irwin

R. F. Frindt
Senior Supervisor

S. R. Morrison

B. P. Clayman

G. Kirczenow
External examiner
Professor
Department of Physics
Simon Fraser University

Date Approved:

PARTIAL COPYRIGHT LICENSE

I hereby grant to Simon Fraser University the right to lend my thesis, project or extended essay (the title of which is shown below) to users of the Simon Fraser University Library, and to make partial or single copies only for such users or in response to a request from the library of any other university, or other educational institution, on its own behalf or for one of its users. I further agree that permission for multiple copying of this work for scholarly purposes may be granted by me or the Dean of Graduate Studies. It is understood that copying or publication of this work for financial gain shall not be allowed without my written permission.

Title of Thesis/Project/Extended Essay

Thermopower of Tantalum Diselenide in the charge density wave regime

Author: _____
(signature)

Sabaratnasingam Gnanarajan
(name)

31 Jan 1985
(date)

ABSTRACT

The thermopower of 2H-$TaSe_2$ crystals was studied in the temperature range 40K to 160K. Above and close to the charge density wave (CDW) transition temperature at 122K the thermopower is positive. On cooling there is a sharp change in thermopower at 122K and the thermopower decreases positively and changes sign below 105K. On warming a large hysteresis is observed between 65K and 110K and a relatively small hysteresis is observed between 110K and 122K. The hysteresis observed in published X-ray studies between cooling and warming above 85K is reasonably consistent with the hysteresis in thermopower, but the thermopower hysteresis exhibited below 85K is not present in the X-ray results. The hysteresis in the thermopower below 85K is compared with the hysteresis exhibited in CDW domain sizes observed by dark field electron microscopy in this temperature range. It is suggested that electron scattering by the CDW domain walls could explain the observed hysteresis.

ACKNOWLEDGEMENTS

I wish to express my deepest gratitude to my supervisor Dr.R.F. Frindt for his guidance, encouragement and patience throughout this research work.

My sincere thanks are due to Per Joenson for his willing assistance and valuable advice.

Many thanks are due to the members of the examining committee Dr.B.P. Clayman, Dr.S.R.Morrison and Dr.G.Kirczenow for reading the manuscript and helpful suggestions, I also wish to thank Dr.D.J.Huntly for the helpful discussions with him.

The financial assistance from my supervisor Dr.R.F.Frindt through a research grant from the Natural Sciences and Engineering Research Council of Canada and the teaching assistantships from S.F.U. is greatfully acknowledged.

I am grateful to the Instructional Media Centre of S.F.U. for the useful suggestions and willing help given to me for the graphical work. My thanks are due to the faculty, the technical staff, the secretarial staff and all other members of the department for their help and friendly cooperation.

Finally I am very thankful to the University of Jaffna, Sri Lanka who made it possible for me to came to the Simon Fraser University.

TABLE OF CONTENTS

LIST OF FIGURES

I. Introduction

1.1 General

The layered transition-metal dichalcogenides and their intercalation complexes have received much attention as a result of their highly anisotropic properties. To a large extent current interest has been promoted by the discovery that many of the metallic layered compounds exhibit charge density wave instablities.

The vast majority of compounds crystalise into a regular lattice in which a unit cell is repeated indefinitley, except for generally localized defects, impurities and boundaries. In a few compounds however, at sufficiently low temperatures this regular array can be unstable with respect to small distortions. The stable state can be one in which the electron density(1,2) along with the ion positions(3) display long period modulations. The period of these modulations may be commensurate or incommensurate with the spacing of the underlying lattice. If the modulation is commensurate then the wave length of the modulation is an integral multiple of a lattice period(or in the reciprocal lattice the lattice wave vector is an integral multiple of the distortion wave vector); that is the atomic displacement gives the crystal a larger unit cell. If the

modulation is incommensurate then the modulation is not an integral multiple of the lattice period; that is no unit cell can contain an exact period of both the wave and the underlying lattice. This thesis is primarily concerned with the charge density waves in 2H-$TaSe_2$ and a study of transport properties such as the electrical resistivity and thermopower.

1.2 One Dimensional Charge Density Waves

The idea that the electronic energy of a metal could be lowered by a charge density wave was first put forward some 30 years ago by Peierls(4) and Frohlich(5). They considered the special case of a one dimensional metal in which the electrons are confined to move only in one dimension, for example, a linear chain of atoms with spacing a. The Fermi surface then consists of two points. A periodic charge modulation with a wave vector $2\underline{q}$ will cause each ion to be displaced to a new equilibrium position (Fig.1.1(a)). If $\underline{q}=\underline{k}_F$ ($\underline{k}_F$ is the reciprocal wave vector corresponds to the Fermi energy level) then the wave vector will exactly span the Fermi surface. The additional periodic potential creates an energy gap at the Fermi surface(Fig.1.1(b)) because electrons whose momenta satisfy the Bragg condition scatter from the lattice modulation. Electron states below the Fermi surface have their energy lowered while those above the Fermi surface have theirs raised; this reduction in electronic energy is the driving force in CDW formation. At

sufficiently low temperatures then nearly all the states that are lowered are filled while those that are raised are empty, and the total energy of the distorted state is lower than the normal state, i.e. a one dimensional metal is inherently unstable against charge density wave formation. Subsequent theoretical work(6) has shown that this instablity is not restricted to one dimensional systems.

Fig.1.1(a) A charge density wave in a one dimensional metal. The graph shows the sinusoidally modulated density of conduction electrons. The dark spots represent the lattice.

(b) Energy vs wave vector relation in the presence of a CDW with a lattice distortion corresponding to $\underline{q}=\underline{k}$ in reciprocal space for 1-D. The energy band develops a gap at the Fermi energy at $|\underline{q}| = \pi/2a$.

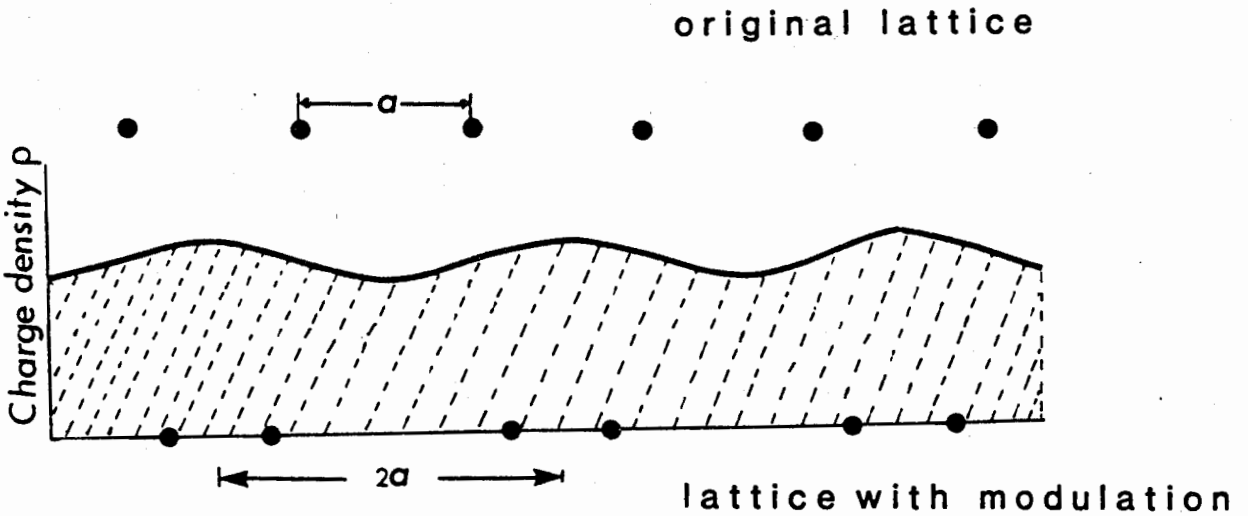
original lattice
a
Charge density ρ
2a
lattice with modulation

(a)

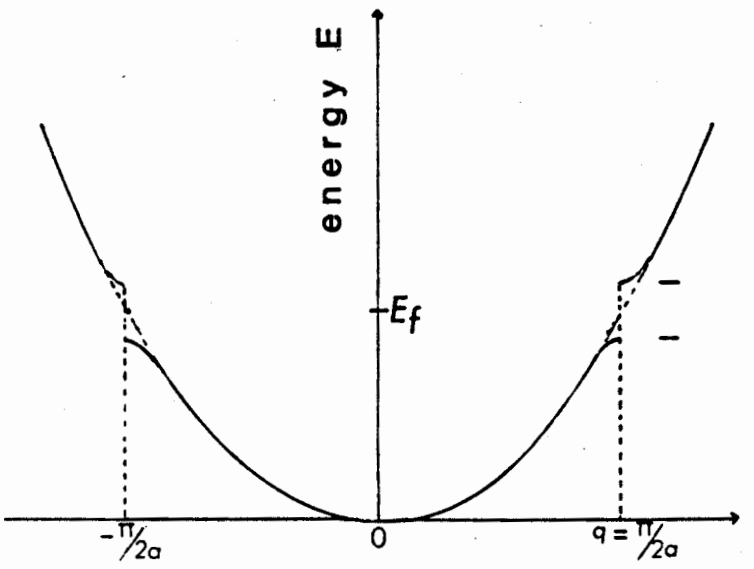
energy E
E_f
$-\pi/2a$
0
$q = \pi/2a$
wavevector k

(b)

FIG.1.1

In the last decade evidence for charge density waves has been found in a number of systems. Several of these systems have essentially one dimensional structures such as potassium cyanoplatinate(KCP), $NbSe_3$, TaS_3 while others such as $TaSe_2$, $NbSe_2$, TaS_2 are approximately two dimensional. A large class of organic compounds also display charge density waves at low temperatures. Charge density wave formation is general to the group VB metal dichalcogenides in large part, it seems, because of the form and the simplicity of the Fermi surface, to which the layered structure of the materials adds a high degree of two dimensionality(1).

The modulation of the lattice sites that accompanies CDW formation may be detected by electron, X-ray or neutron diffraction. New diffraction satellites appear separated from each Bragg vector $\underline{G}$ of the underlying lattice by $2m\underline{q}$, where m is an integer. In Fig.1.2 the open circles are due to Bragg scattering and the solid circles are due to lattice distortion. The wave length of the lattice distortion is 3 times the lattice spacing in the real space i.e in the reciprocal super lattice the lattice distortion wave vector is 1/3 of the lattice wave vector. The location of these new satellites serves to determine the period of the CDW distortion, $\pi/|\underline{q}|$, and for small lattice modulations the satellite intensity is proportional to $((\underline{G}+2m\underline{q}).\underline{u})$,where $\underline{u}$ is the amplitude of the lattice modulation(1). The wave vector of the lattice distortion in reciprocal space can be written as $(1-\delta)\underline{G}/n$, where n is an

integer and δ is a measure of incommensurablity of the lattice distortion as indicated in Fig 1.2(b).

While diffraction experiments were able to show that the ions move they did not directly show that the local charge at each ion is modulated. To measure this local charge one needs a probe sensitive to the distribution of conduction electrons. X-ray spectroscopy is such a probe. By measuring the absolute energy of a core level the local electronic environment of the ion can be detected. Another probe that can give information about electron densities is nuclear magnetic resonance(NMR). The nuclear resonance frequency is determined by the applied magnetic field and by the internal magnetic fields due to the spin and orbital magnetic moments of the conduction electrons. These fields give rise to a small shift in the resonance frequency of each nucleus, called the Knight shift, which is proportional to the conduction electron density at each nucleus. Furthermore, if the nuclear spin is greater than 1/2, satellites may appear around the main resonance due to splitting of nuclear quadrupole levels by local electric fields.

Fig.1.2 (a) $\underline{G}/3$ reciprocal superlattice.
Where $\underline{G}$ is the smallest vector
joining the open circles (the Bragg points
of the 2H-structure). The wave vectors
$\underline{q}_1$, $\underline{q}_2$, $\underline{q}_3$ characterize the lattice distortion.

(b) The reciprocal lattice in the $\underline{q}$ direction for
the commensurate and the incommensurate case.
The δ shown is a measure of incommensurablity.
(δ is defined in section 1.2)

RECIPROCAL SUPERLATTICE

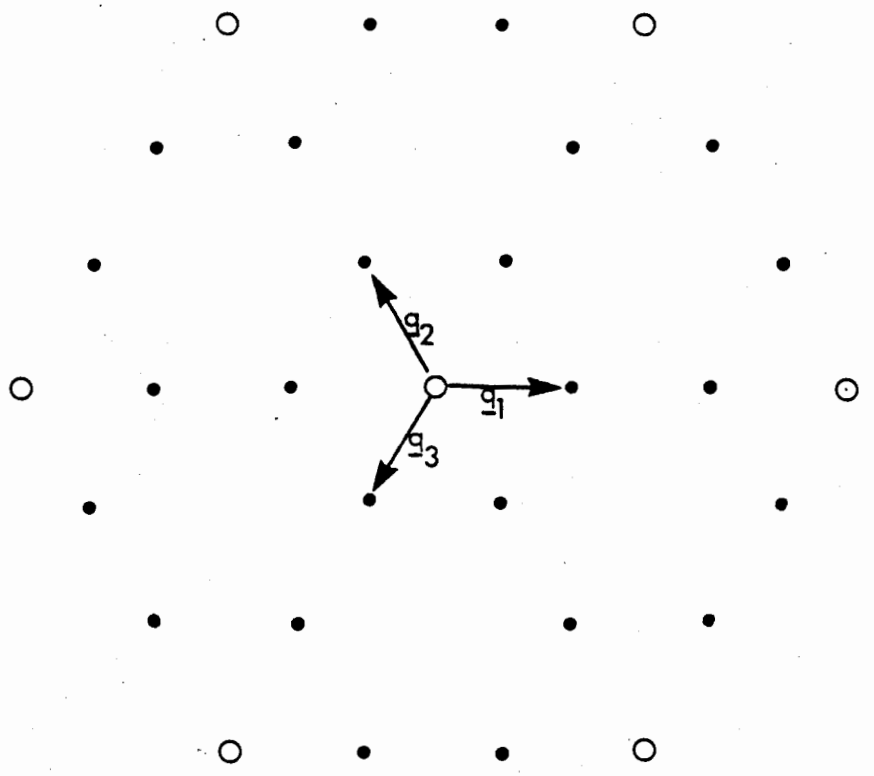

(a)

(b)

FIG.1.2

1.3 Structure and Properties of Layered Compounds

1.3.1 General Considerations

2H-$TaSe_2$ belongs to a family of layered transiton metal (from groups IVB,VB,VIB) dichalcogenides. The structure and properties of the layered compounds were summarised in an early review paper by Wilson and Yoffe(7). These compounds have the formula TX_2, where T is the transition metal atom from group IVB, VB or VIB columns of the periodic table and X is one of the chalcogens, sulfur, selenium or tellurium. Structurally, these compounds form strongly bonded two-dimensional layers or sandwiches which are loosly coupled to one another by relatively weak Van der Waals-type forces. Within a single X-T-X sandwich, the T and X atoms form two-dimensional hexagonal arrays. For this reason the names "layer material" and "layer compounds" are also used for layer transition-metal dichalcogenides.

There are several types of polytypes in the layer materials, especially in the group VB materials and depending on the stacking sequence they have different abbreviated notations. Most of the members of the other groups (IV, VI) fall into just one coordination class:the trigonal prismatic coordination.

1.3.2 General Properties

A total of about 60 layer compounds make up the transition-metal dichalcogenides. These compounds exhibit a wide range of properties. Electrically most of the group IVB and VIB compounds are semiconductors (some of them are semi-metals and insulators), while group VB compounds are mostly metals. Most of the Nb and Ta compounds are supercoductors and exhibit a large anisotropy due to weak inter-layer coupling. For example, for the metallic compounds, the room temperature conductivity parallel to the layers is typically 30 to 50 times larger than that perpendicular to the layers.

1.4 Structure and Properties of 2H-$TaSe_2$

1.4.1 Structure of $TaSe_2$

$TaSe_2$ has seven polytypes labelled 1T, 2H, 3R, 4Ha, 4Hb, 4Hc, 6R (7). In this abbreviated notation, the integer indicates the number of layers per unit cell along the hexogonal symmetry axis (c or z), and T, H and R denote the trigonal, hexagonal and rhombohedral primitive unit cells respectively. In the 1T polytype of $TaSe_2$, for example, the Ta atom is octahedrally coordinated by sulphur atoms while in the 2H phase the coordination is trigonal prismatic. In the the 4Hb and 6R polytypes, the coordination within the successive layers alternates between octahedral and trigonal prismatic(7). The 2H

structure of $TaSe_2$ with crystal parameters and the conventional unit cell ($11\bar{2}0$ section) are shown in Fig.1.3(a) and Fig.1.3(b) respectively.

Fig.1.3 (a) 2H-structure and crystallographic parameters for 2H-$TaSe_2$.

(b) Conventional unit cell ($11\bar{2}0$ section) of 2H-$TaSe_2$.

2H-$TaSe_2$ CRYSTAL STRUCTURE

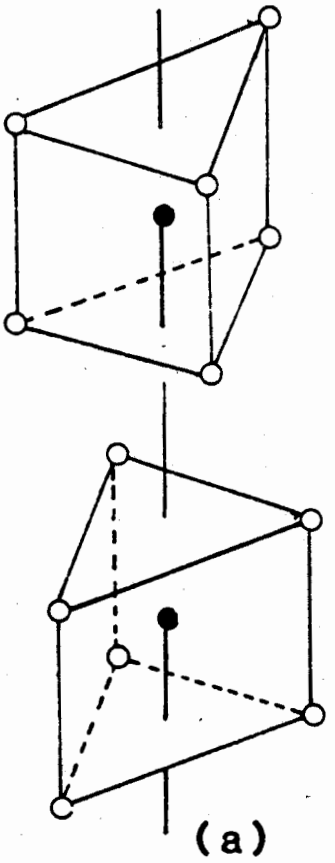

Ta- ●

Se- ○

a=3.436Å

c=12.70Å

(a)

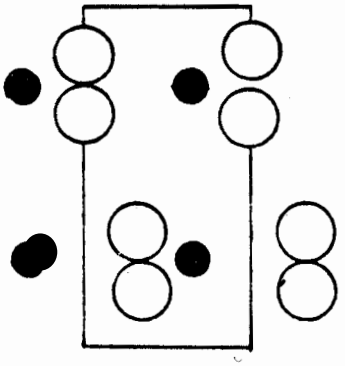

1120 section

(b)

FIG.1.3

1.4.2 General Properties of 2H-$TaSe_2$ in the CDW Regime

Of the various layered CDW systems, the 2H polytype of $TaSe_2$ has been most thoroughly investigated. The system is very rich in the sense that each increase in the resolution or sophistication of the probe has uncovered more subtle behavior. The electrical resistivity and magnetic susceptibility show anomalous behavior near 122K and have been explained in terms of CDW formation(8). Preliminary elastic measurements revealed, in addition to a weak anomaly near 122K, a large elastic modulus minimum and internal friction maximum near 90K which suggested a second phase transition(9). By contrast previous resistivity and magnetic susceptibility measurements showed only slowly varying behavior near 90K. Subsequently high precision neutron scattering measurements showed that CDW's in 2H-$TaSe_2$ are actually a few percent out of commensurability at the onset temperature (T=122.3K)and the elastic anomalies near 90k are associated with the lock-in or commensurate transition(9).

1.4.3 The Resistivity of 2H-$TaSe_2$

The resistivity vs temperature curve for 2H-$TaSe_2$ is shown in Fig.1.4(a). Other work on resistance measurements by B.H.Suits *et al*(14) shows that the derivative of the measured sample resistance exhibits bumps around 90K and hysteresis in resistivity of about 0.6%. At about 110K to 112K a bump occurs on the heating cycle but is absent on the cooling cycle.

Fig.1.4(b) shows the hysteresis of the measured resistance as a function of temperature. Between about 88K and 93K the hysteresis curve exhibits a peak which is due to the difference in resistivity of the commensurate state and an incommensurate state. This is the temperature region where the commensurate-incommensurate transition was observed by Fleming et al(11) (see section 1.5).

Fig.1.4 (a) Log-log plot of resistivity for 2H-$TaSe_2$.
(After Naito et al(10))
(Resistance ratio of the crystal
R(300)/R(4.2)=200)

(b) Temperature dependence of hysteresis in resistance for 2H-$TaSe_2$. The hysteresis was taken positive when the resistance on cooling is larger the resistance on heating.
(After Suits et al(11))

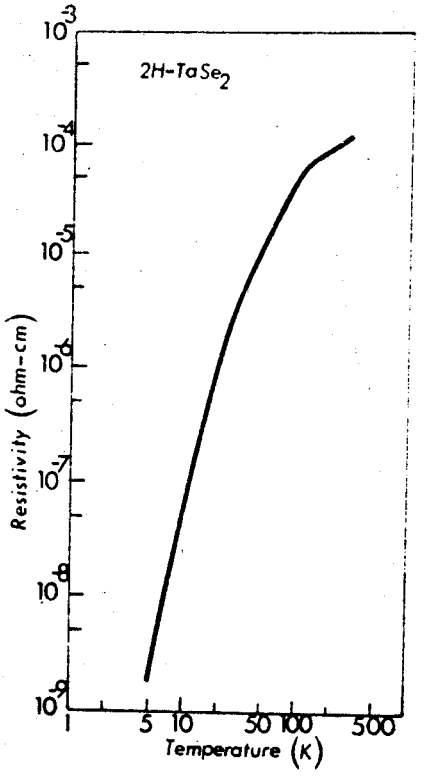
2H-TaSe2
Resistivity (ohm-cm)
Temperature (K)
5
10
50
100
500

(a)

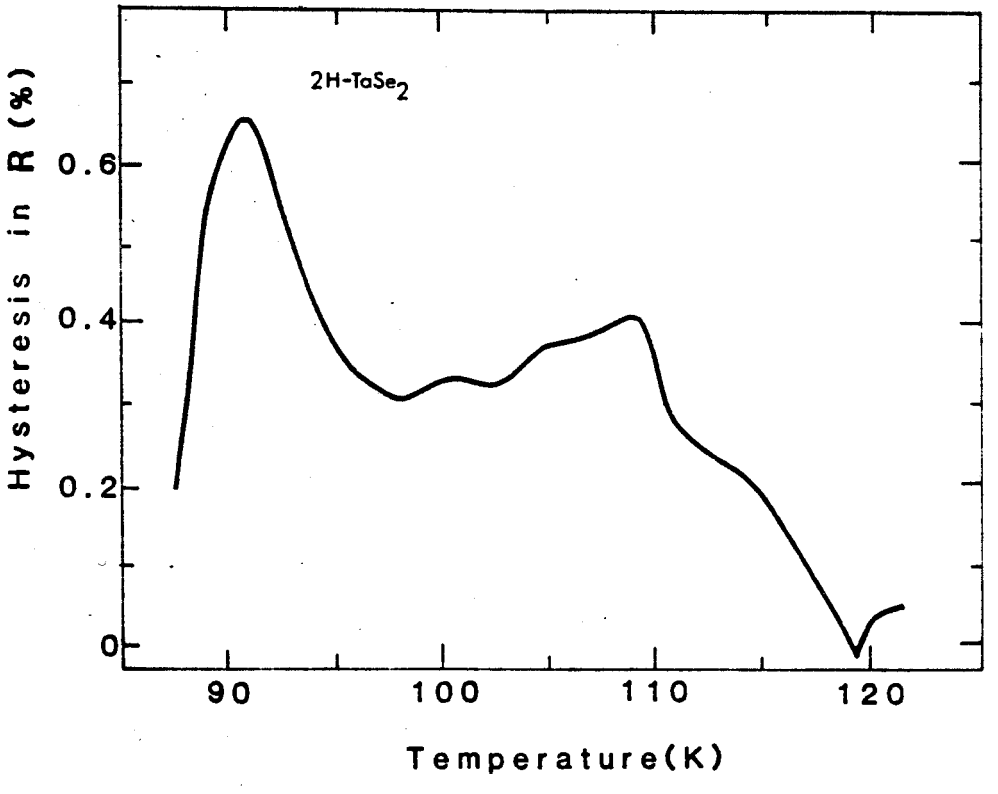
2H-TaSe2
Hysteresis in R (%)
0.6
0.4
0.2
0
90
100
110
120
Temperature(K)

(b)

FIG.1.4

1.4.4 The Hall coefficient of $2H\text{-}TaSe_2$

The Hall coefficient of $2H\text{-}TaSe_2$ at room temperature is 1.6×10^{4} cm^3/C. The Hall coefficient(R_H) vs temperature curve in Fig.1.5 shows that above the transition temperature 122K R_H is nearly constant. Below 122K with the onset of CDW formation, R_H decreases gradually and changes sign at about 105K. It has a minimum around 30K and then increases at low temperatures. Note that the sign of the Hall coefficient is positive above the CDW transition region. No hysteresis has been reported in the Hall coefficient results.

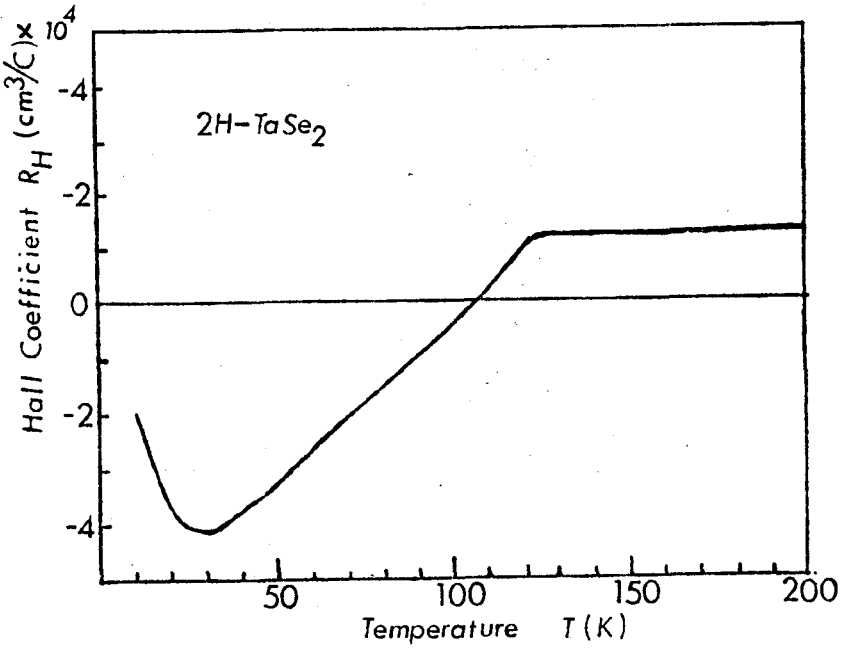

Fig.1.5 Temperature dependence of Hall coefficient for $2H\text{-}TaSe_2$.
(After Naito et al(10))

1.5 Lattice Structure for 2H-$TaSe_2$ in the CDW State

Early electron diffraction studies(1) showed satellite reflections appearing at $T \leq T_0 = 123K$. Initially these peaks were thought to be commensurate with a reduced wave vector $\underline{q}=\underline{G}/3$ but a subsequent higher resolution neutron scattering study by Moncton et al(16) showed the structure to be incommensurate near T_0 with wave vector $\underline{q}=(1-\delta)\underline{a}/3$. Just below 123K δ had the value 0.02 and was shown to drop smoothly upon cooling to T=90K where δ went rapidly to zero. Both the incommensurate and commensurate phases exhibited hexagonal symmetry on a macroscopic scale. For the commensurate and the fully incommensurate states discussed above, the CDW modulation is a coherent superposition of identical components with wave vectors ($\underline{q}_1$, $\underline{q}_2$, $\underline{q}_3$), along each of the hexagonal symmetry axes.

The next discovery came in a high resolution X-ray study by Fleming et al(Fig.1.6(a))(11). On cooling below T=122K the CDW is fully incommensurate and the incommensurablity approaches zero continuously down to 85K (T_{c1}). This phase can be thought of as characterised by regions separated by a hexagonal(honeycomb) pattern of domain walls or discommensurations (DC's) in which the phase of the CDW slips relative to a perfectly locked in CDW. On warming they found a new incommensurate CDW structure which could only be obtained upon warming and which manifested itself through a splitting of the CDW satellites on a scale unresolved in the previous studies. This new phase was stable on

warming from 93K (T_{cs}) to 112K (T_{si}) and displayed a clear lack of hexagonal symmetry. The new phase had three nonequivalent coexisting wave vectors, two incommensurate and one commensurate. The one incommensurate wave vector implied a linear or striped arrangement of discommensurations and has been called the "striped phase". The relative stability of striped vs hexagonal domain patterns had been discussed by Bak et al(14), and rests (at T=0) on an argument of competition between wall touching energy (nonexistent for a striped phase) and wall-wall repulsion (for the same density of parallel DC's they are further apart for the honeycomb). At finite temperatures there is a greater entropy associated with the honeycomb. Thus below T_{si} the fully incommensurate phase is metastable and the transformation is discontinuous, as predicted theoretically(14). The onset transformation at T appears continuous but is expected theoretically to be 1st order(14). The transformations at T_{ci}(on cooling) and T_{cs}(on warming) appear continuous but only the latter is predicted to be so(14).

Fig.1.6 (a) Temperature dependence of incommensurablity, δ, in 2H-$TaSe_2$. On cooling only the fully incommensurate phase appears. On warming an additional phase is present between T = 93K and T = 112K. In this figure, δ is in units of G/3
(After Fleming et al(12))

--- cooling

—— warming

(b) The commensurate phase resulting from the CDW components in a single layer of 2H-$TaSe_2$. Atomic positions are projected onto a single plane parallel to the layer. Solid lines represents maxima of the CDW's.
(After Walker et al(17))

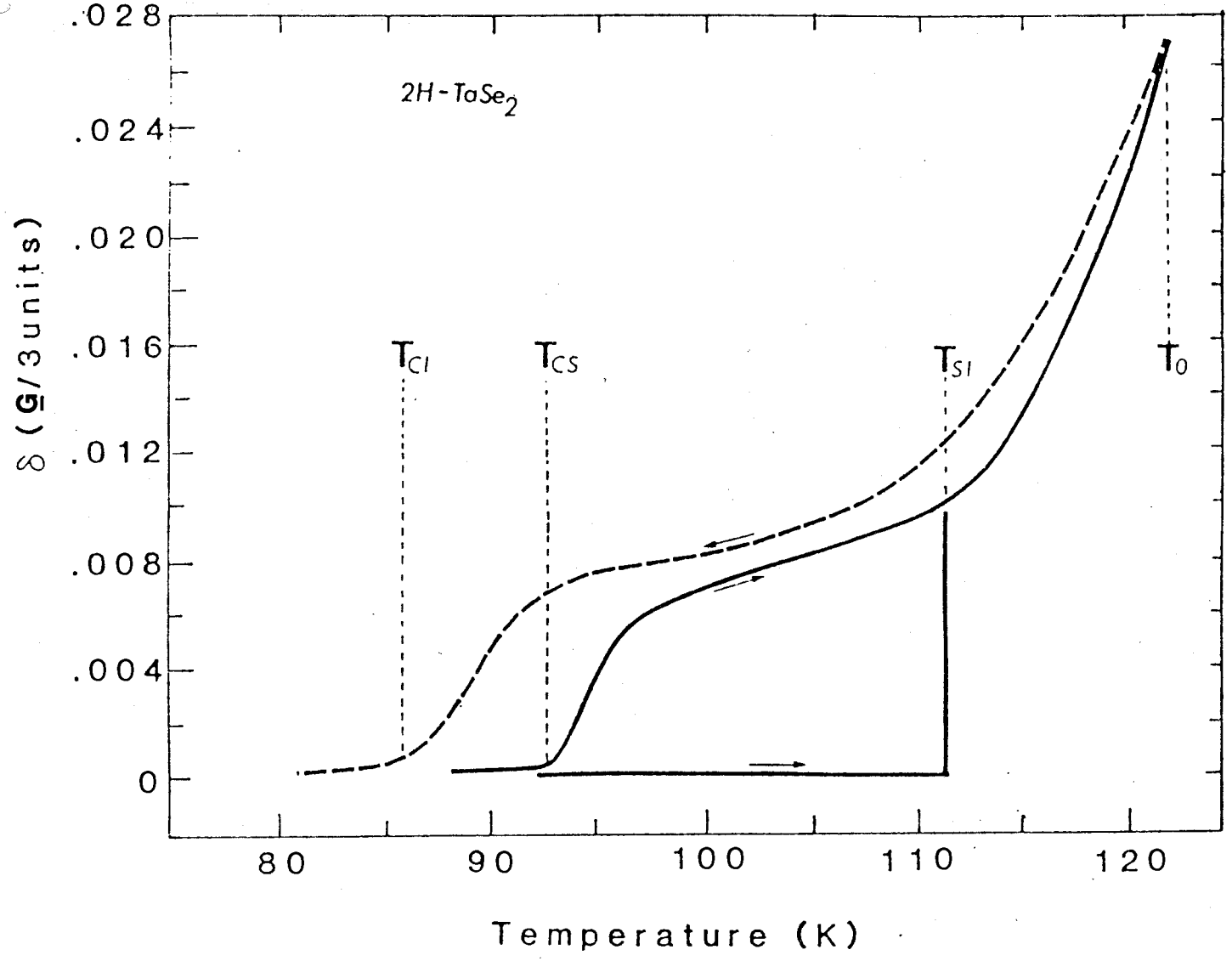
2H - TaSe2
.028
.024
.020
.016
.012
.008
.004
0
δ (G/3units)
TCI
TCS
TSI
T0
80
90
100
110
120
Temperature (K)

FIG. 1.6(a)

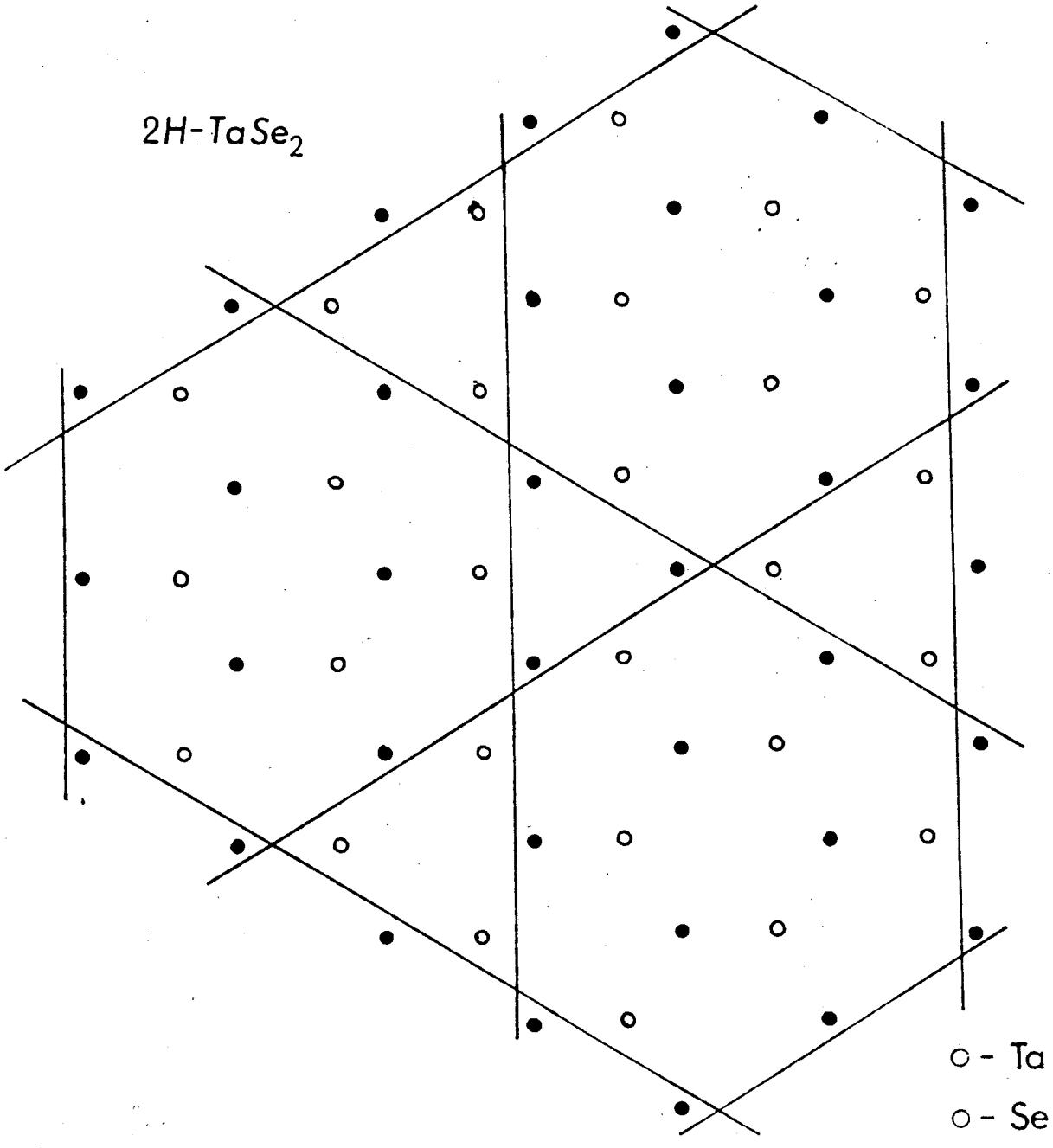

FIG. 1.6 (b)

The next round of revelations came from the direct imaging(15,16) of domain microstructure using superlattice dark field electron microscopy on thin film samples with a thickness of 1000Å. The first surprise was that the commensurate phase although hexagonal on a macroscopic scale consisted of rather large (1 μm) domains having orthorhombic symmetry. Details of electron microscopic results are given in the next section. The explanation of the broken hexagonal symmetry is rather subtle. The distortions for a single layer were analysed by Walker et al (17,18). By assuming the superposition of three plane wave CDW's with amplitude $=\underline{G}/3.e^{i\phi_j}$ ($j=1,2,3$ associated with equivalent wave vectors $\underline{q}_j$), three structures were considered to be possible. The different choices of ϕ_j are obtained by shifting the position of the 3-fold axis within a single layer. In each case the distorted layer retains hexagonal symmetry, but there are two layers per unit cell and the resultant pattern can have lower symmetry. But only the structure shown in Fig 1.6(b) is compatible with NMR(19) and Mossbauer studies(20) as well as electron microscopy.

On warming above T_{cs}, alternate regions of dark and bright stripes are observed to nucleate within each orthorhombic domain(16). The average width of the stripes changes with temperature in a manner that is consistent with the X-ray diffraction measurements of the incommensurability.

1.5 Electron Microscope Domain Imaging

The following is a summary of the observations made by Chen et al(16) using dark field electron microscopy. Dark field images are formed by encircling strong satellite reflections from a convergent beam electron diffraction pattern due to the CDW and excluding all other reflections.

(a) Cooling

On cooling below the CDW transition temperature (122K), at 115K parallel stripes 200Å apart were seen at an angle $\pi/2$ to the imaging q direction. At 110K another set of stripes at an angle $2\pi/3$ to the original set showed up. As a result of the intersection of the two sets of stripes, the image of the stripes becomes fragmentary and less smooth. As the temperature decreases further, the stripes became wavy and jagged domains appeared. At 85K some diamond shape domains are apparent (Fig 1.7(a)). At 80K some of the jagged domains combined into large domains(Fig 1.7(b)). Further combinations of domains occur at a lower temperature of 75K as shown in Fig 1.7(c) and no changes of the domain structure were seen below 65K. The size of the domains was non uniform and changed from a few hundred angstroms to 1 μm on cooling.

(b) The commensurate phase (T≤85K)

Electron micrographs taken from any CDW super lattice reflection in the commensurate phase below 85K revealed many large (1 μm size) dark domains separated by sharp boundaries. The dark domains appeared to have orthorhombic symmetry instead of the hexagonal symmetry previously suggested by the X-ray diffraction studies. These domains can be oriented in three different directions.

(c) Warming

On warming no significant changes of the domain pattern between 20K to 80K were observed(Fig 1.8(a)). As the temperature approached the commensurate/striped-phase transition around 92K, stripes were found to nucleate within the orthorhombic domains (Fig 1.8(b)). Domain boundaries became mobile in the temperature range 80-90K.

(d) Warming and cooling between 50-95K

An area which was heated up to 95K (in the striped phase regime) and cooled down to 80K showed many stripes. These stripes combined into bigger domains upon further cooling. A sample which was cooled down to 50K and then warmed up to 80K showed different patterns from the previous one (this observation is used in the explanation of hysteresis effects observed in this thesis)

According to their results Chen et al concluded that all the stripes in the striped phase have orthorhombic symmetry. On cooling Chen et al showed the honeycomb array of domains and discommensurations in the incommensurate phase (mentioned earlier in sec 1.5) is not consistent with their results. According to their results, on the microscopic scale orthorhombic symmetry is predominant over most of the temperature range in the incommensurate CDW state. Only at temperatures greater than 115K, is the existence of the hexagonal symmetry state of incommensurate CDW's possible.

Fig.1.7 Schematic drawing of the microstructure in the incommensurate and the commensurate CDW domains observed by electron microscopy at different temperatures when cooling. The region with stripes in Fig.1.7(a) is the incommensurate region and the blank regions in Fig.1.7 (b) and (c) are the Commensurate regions.
(After Chen et al(16))

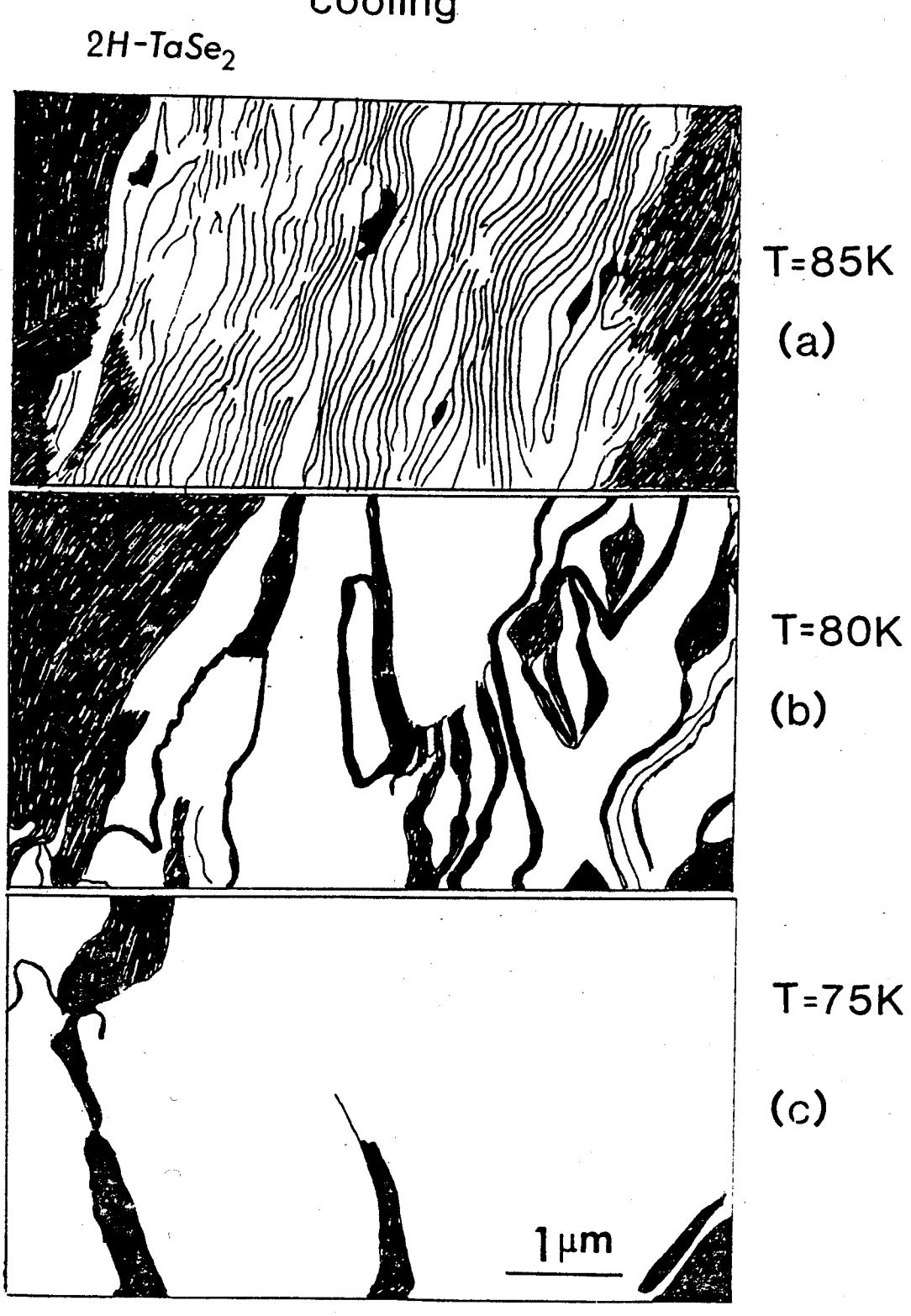

FIG.1.7

Fig.1.8 Schematic drawing of the microstructure in the commensurate CDW domains observed by electron microscopy at different temperatures when warming.
(After Chen *et al*(16))

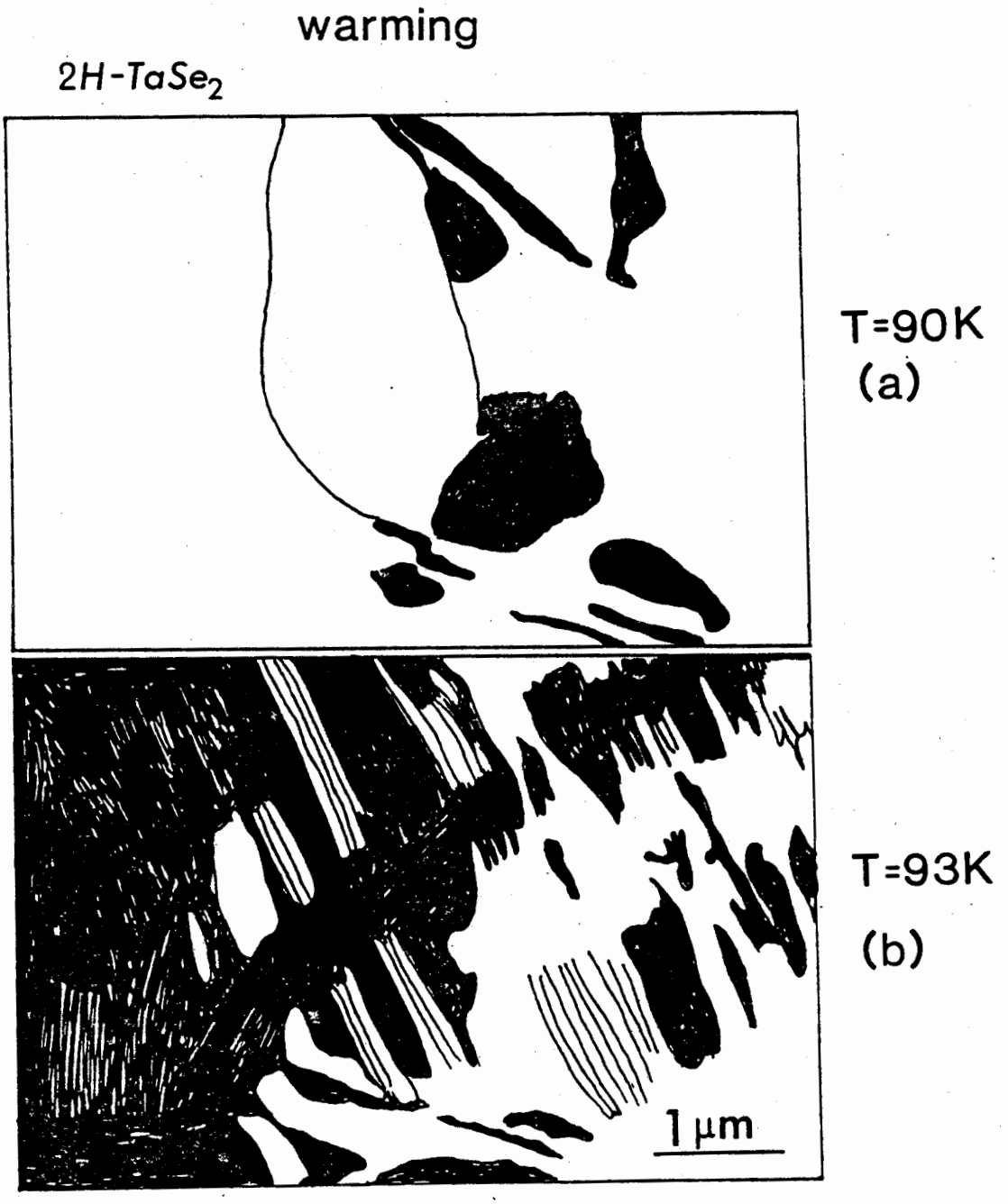

FIG.1.8

1.6 Motivation

After the discovery(21) of large non-ohmic resistance effects in $NbSe_3$, it was shown by x-ray diffraction on samples carrying an electric current that this effect was due to charge transport by a sliding charge density wave(22). Further measurements have also shown that the charge density wave moves only when the electric field is greater than a threshold field (depinning field). However, within the class of materials known to exhibit CDW phases only $NbSe_3$ and TaS_3 have been shown to display non-ohmic behavior. The work in this thesis was motivated by a desire to see if similar non-linear effects in the resistance were present in 2H-$TaSe_2$. Such a search was done earlier by Disalvo et al(23) but they did not observe any nonlinear effect in resistivity for electric fields up to 1V/cm for crystals of 0.1mm thick.

However in this work a search was done on thin samples for similar behavior. In thin samples the temperature and current through the sample can be controlled easily. It was found that electric fields of 10 V/cm could be achieved before sample heating effects were apparent and there was no nonlinear behavior observed up to this field. A search was also done with very small currents (current density $\sim$ 1 A/cm^2) and it was observed that there is a thermo-electric potential which changes abruptly at the CDW transition temperature. This observation led to the measurement of thermopower in 2H-$TaSe_2$ in the CDW regime.

II. Thermopower

2.1 Thermoelectricity

Thermoelecticity concerns the generation of an E.M.F by thermal means. This involves subjecting a conductor to a temperature gradient. Physically, in a metal the phenomenon arises because electrons at the hot end of the metal can find states of lower energy at the cold end. Thus the electrons diffuse to the cold end setting up an electric potential difference between the two ends of the conductor.

2.2 The Seebeck Effect

When we speak of the Seebeck effect we generally envisage an open circuit, such as that shown in Fig.2.1, where A and B are two dissimilar metals.

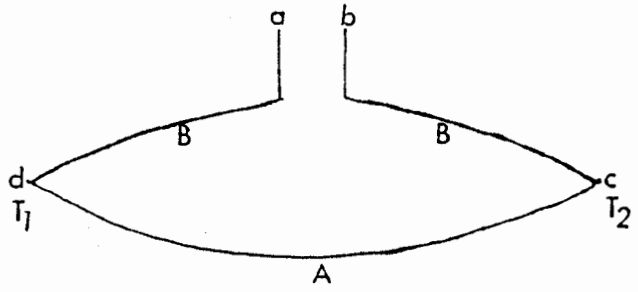

Fig.2.1 Thermocouple

A voltage $\Delta V = V_b - V_a$(the thermoelectric potential) is developed

by this couple and the thermopower of the couple, is defined by

$$S = \lim_{\Delta T \to 0} \Delta V/\Delta T$$

The terminals a and b are assumed to be at the same temperature and the junctions c and d at temperatures T_2 and T_1 as shown. Although the thermopower of a couple evidently involves the difference in the response of two dissimilar metals to a temperature gradient, it is nevertheless possible, and also convenient to define the absolute thermopower S, which is a unique physical property of a particular material, by the relation.

$$\underline{E} = S\underline{\nabla}T \text{ ---------- } (1)$$

Where $\underline{E}$ is the electric field in the material and ΔT the temperature gradient. Since $\underline{E}$ and $\underline{\nabla}T$ are vector quantities, S is generally a tensor. For simplicity we will consider here isotropic systems.

From equation (1) we have $-\underline{\nabla}V = S\underline{\nabla}T$ or $dV = -SdT$

So $V = V_b - V_a = (V_b - V_c) + (V_c - V_d) + (V_d - V_a)$

$$= -\int_c^b S_B\,dT - \int_d^c S_A\,dT - \int_a^d S_B\,dT$$

$$= -\int_c^d S_B\,dT - \int_d^c S_A\,dT$$

$$= \int_{T_1}^{T_2} (S_B - S_A)\, dT \text{ --------- (2)}$$

Evidently the thermopower of the couple defined by equation (2) is given by

$$S_{AB} = S_B - S_A \text{ -------- (3)}$$

and hereafter S_A and S_B are called absolute thermopowers of metals A and B respectively.

2.3 Derivation of Thermopower using the Transport Equation

A very much simplified model of the perfect crystal is a regular array of positive ions embedded in a "gas" of electrons, whose average charge density is such as to maintain macroscopic electrical neutrality. In this model we view the electron gas as an assembly of noninteracting charged particles of spin one-half, obeying Fermi-Dirac statistics. As regards the lattice of positive ions the dominant features here are the spatial periodicity and point symmetry of the lattice.

The conduction electrons feel the presence of the ions through their mutual coulomb interaction. This interaction may be separated into two terms, one time independent and the other time dependent. The time dependent part of the interaction arises from the oscillatary motion and leads to the scattering of the electrons due to absorption or emission of phonons which is not considered here. The time independent spatially periodic

part is of fundamental importance and it gives rise to the Brillouin zone structure and the appearance of electronic energy bands in solids.

The quantity $\hbar\underline{k}$ is referred to as the crystal momentum of the electron partly because under the influence of the external driving force, $\underline{F}$, the wave vector $\underline{k}$ changes with time according to

$$\hbar\dot{\underline{k}} = \underline{F} \text{---------- (4)}$$

The velocity of the electrons $\underline{V}(\underline{k})$ in state $\underline{k}$ is given by the expression

$$\underline{V}(\underline{k}) = 1/\hbar.\underline{\nabla}_k \epsilon(\underline{k}) \text{ ------- (5)}$$

where $\epsilon(\underline{k})$ is energy of the electron in state $\underline{k}$.

Expressions for the transport coefficients are derived by solving the Boltzmann transport equation(32) subject to appropriate boundary conditions. Under steady state conditions in a bulk sample the distribution function f must satisfy the equation

$$\dot{\underline{k}}.\underline{\nabla}_k f + \underline{V}(\underline{k}).\underline{\nabla}_r f = (\partial f/\partial t) \text{ --- (6)}$$

where $\underline{\nabla}_r = (\partial/\partial x, \partial/\partial y, \partial/\partial z)$

and $\underline{\nabla}_k = (\partial/\partial k_x , \partial/\partial k_y , \partial/\partial k_z)$

The term on the right hand side is the collision term which gives the number of electrons scattered into the six-dimensional volume element dk^3dr^3 per unit time. In many situations however the collision term can be approximated by means of a relaxation time, τ.

$$(\partial f/\partial t) = -(f-f_0)/\tau = -f_1/\tau \text{ --- (7)}$$

where f_0 = Equilibrium distribution of electrons
when there are no external forces
and τ will generally be a function of electron energy.

The only external force present here is the electric field $\underline{E}$. The perturbations produced by the electric field and the temperature gradient on the electron system are usually very small so that the perturbed distribution function f is not greatly different from f_0. The difference is important only on the right hand side of the equation (6).

$$\text{i.e.} \underline{\nabla} f \simeq \underline{\nabla} f_0$$

$$\text{then } -f_1/\tau(\underline{k}) = e/\hbar . \underline{E} . \underline{\nabla}_k f + \underline{V}(\underline{k}) . \underline{\nabla}_r f \text{ ---- (8)}$$

The electron current density $\underline{J}$ is given by

$$\underline{J} = e/(4\pi^3) \iiint \underline{V}(\underline{k}) f \, dk^3 \text{ ---(9)}$$

where dk^3 is a volume element in $\underline{k}$ space

The heat current density $\underline{U}$ is given by

$$\underline{U} = 1/(4\pi^3)\iiint \underline{V}(\underline{k})(\epsilon - \mu)f^3{}_0 dk^3 \quad ----(10)$$

μ = chemical potential

It is reasonable to assume $\mu = \epsilon_F$ for normal temperatures.

If we consider the field and temperature gradient in the x-direction only then equation (8) becomes

$$-f_1/\tau(\underline{k}) = e/\hbar . E_x \partial f_0/\partial k + V_x(\underline{k}).\partial f_0/\partial x \quad ---(11)$$

where $\underline{E}$ is the electric field. Thus using

$$\partial f_0/\partial x = \partial f_0/\partial T \; . \; \partial T/\partial x$$

$$= \partial f_0/\partial \epsilon . \partial \epsilon/\partial Y . \partial Y/\partial T . \partial T/\partial x$$

where $Y = (\epsilon - \epsilon_F)/k\,T$, We have that

$$\partial f_0/\partial x = \partial f_0/\partial \epsilon . T . \partial/\partial T \; (\epsilon - \epsilon_F)/T . \partial T/\partial x$$

$$= \partial f_0/\partial \epsilon [-\epsilon/T + \epsilon_F/T - \partial \epsilon_F/\partial T] \; \partial T/\partial x \; -- \; (12)$$

Equations (11) and (12) give

$$-f_1/\tau(k) = e/\hbar . E_x \partial\epsilon/\partial k + V_x(\underline{k})(-\epsilon/T + \epsilon_F/T - \partial\epsilon_F/\partial T)\ \partial T/\partial x . \partial f_0/\partial\epsilon \quad \text{--- (13)}$$

The volume integral with respect to $\underline{k}$ can be changed to one of ϵ.

$$dk^3 = dk_1 dk_2 dk_3$$

can be written as $dk^3 = d\underline{A} dk_3$,

where $d\underline{A}$ is an elemental Fermi surface area

Then $dk^3 = d\underline{A}(\partial k_3/\partial\epsilon)\ d\epsilon = d\underline{A} d\epsilon/\underline{\nabla}\epsilon$

Then J_x (Eq 9) and U_x (Eq 10) can shown to be given by

$$J_x = (e^2 M_0)E_x + |e|[(\partial\epsilon_F/\partial T - \epsilon_F/T)M_0 + 1/T\ M_1]\partial T/\partial x \quad \text{--- (14)}$$

$$U_x = -(|e|M_0)E_x - [(\partial\epsilon_F/\partial T - \epsilon_F/T)M_0 + 1/T\ M_1]\partial T/\partial x \quad \text{--- (15)}$$

where

$$M_n = -1/(4\pi^3\hbar^2)\int\epsilon^n\ \partial f_0/\partial\epsilon[\int\int(\partial\epsilon/\partial k)\tau(k)/\underline{\nabla}_k\epsilon . d\underline{A}]d\epsilon \quad \text{--- (16)}$$

Under isothermal conditions the electrical conductivity in the X-direction (σ_x) is defined by

$$\sigma_x = J_x/E_x$$

Then equation (14) gives

$$\sigma = e^2 M_0$$

The thermopower in the X-direction (S_x) is defined by

$$S_x = E_x/(\partial T/\partial x)$$

Then equation (14) gives

$$S_x = -1/|e| . T(M_1/M_0 - \epsilon_F)$$

To first order

$$\sigma_x = e^2/(4\pi^3\hbar^2) \iint (\partial\epsilon/\partial k)\tau(\underline{k})/\underline{\nabla}\epsilon \; d\underline{A} \quad \text{---- (17)}$$

$$S_x = -\pi^2 k^2 T/3|e| [\partial/\partial\epsilon(\ln\sigma(\epsilon))]_{\epsilon=\epsilon_F} \quad \text{--- (18)}$$

S_x also can be written in terms of the mean free path l.

In the case of a spherical Fermi surface with isotropic τ

$$(\partial\epsilon/\partial k_x)^2 = \hbar^2 V_x^2 = 1/3\,(\hbar^2 V_k^2) \text{ and } \underline{\nabla}_k \epsilon = \hbar V_k$$

Then $\sigma_x(\epsilon) = e^2 V\tau/(12\pi^3\hbar) \iint d\underline{A}$,

the integral being taken over the Fermi surface

or $\sigma_x(\epsilon) = e^2/(12\pi^3\hbar).lA$ --- (21)

where $l = \tau V_k$ is the mean free path of the electrons and A is the area of the Fermi surface.

This expression for the conductivity is equivalent to the well-known conductivity equation.

$$\sigma_x = Ne^2\tau/m$$

where N is the number of conduction electrons per unit volume.

For, $l = \tau V \simeq \tau.\hbar k_F/m$ and $A = 4\pi k_F^2$

i.e. $\sigma_x(\epsilon) = e^2\tau/m \; . \; k_F^3 \; /3\pi^2$

but $k_F^3 \; /3\pi^2 = N$,

hence $\sigma_x(\epsilon) = Ne^2\tau/m$

Inserting equation (21) into equation (18) yields

$$S_x = -\pi^2k^2T/(3|e|)[1/A.\partial A/\partial\epsilon + 1/l.\partial l/\partial\epsilon]_{\epsilon=\epsilon_F} \text{ --- (22)}$$

This expression holds for both electron and hole surfaces.

For the thermopower S given by equations (18) and (22) a linear variation with temperature is predicted. From the

expression in equation(18) the sign of the thermopower depends on how the conductivity changes with electron energy at the Fermi surface. In general we expect the conductivity to increase with increasing energy of the electrons so that the thermopower is negative. For the expression of S_x in equation(22) the sign of the thermopower depends on how the area of the Fermi surface and mean free path change with electron energy(ϵ). For electron surfaces the area is expected to increase with ϵ and in general $1/l.\partial l/\partial\epsilon$ is positive since the more energetic the electron the less likely it is to be scattered and the longer should be its mean free path(26) so that the thermopower is negative. On the other hand, for hole surfaces the area of the Fermi surface is expected to decrease with ϵ so that the thermopower can be positive or negative depending on whether $1/l.\partial l/\partial\epsilon$ greater or less than $1/A.\partial A/\partial\epsilon$. A simple example of the situation envisaged is shown in Fig.2.2 where the Fermi surface is spherical but the factor $1/A.\partial A/\partial\epsilon$ is now definitely negative and contributes positively to S. This is clear from Fig.2.2 since a higher energy electron surface results in a smaller hole surface. If the magnitude of $1/A.\partial A/\partial\epsilon$ is larger than $1/l.\partial l/\partial\epsilon$ then a positive diffusion thermopower will result. Thus in general it can be expected that hole carriers contribute to a positive thermopower.

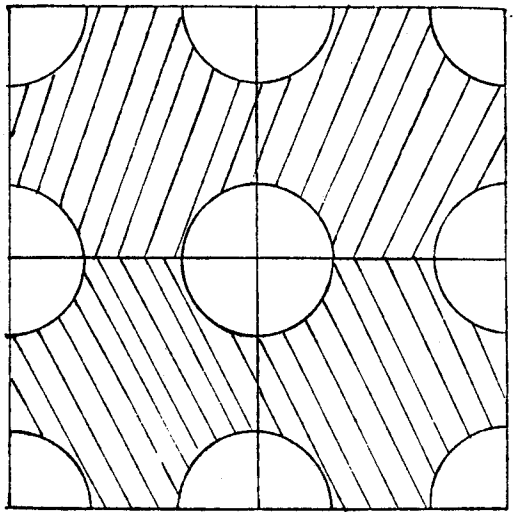

Fig.2.2 Hypothetical spherical hole surfaces.

In most metals the Fermi surface is not spherical, $\tau(\underline{k})$(relaxation time) and $\underline{V}(\underline{k})$ (the electron velocity) are anisotropic so that the simple conductivity expression in equation (21) cannot be applied. In some cases it is possible as a first approximation to divide the Fermi surface into two or more essentially spherical regions which are characterized by isotropic velocities and relaxation times. It can be shown(28) that the conductivity resulting from a division into i spherical Fermi surface regions is

$$\sigma_{\infty} = e^2/(12\pi^3\hbar).\Sigma l_i A_i$$

Then from equation(18),

$$S_x = -\pi^2 k^2 T/(3|e|).\partial/\partial\epsilon(\Sigma l_i A_i)/(\Sigma l_i A_i) \text{--- (23)}$$

If $S_{x,i}$ and $\sigma_{x,i}$ are the thermopower and electrical conductivity associated with spherical region i, then

$$S_{x,i} = -\pi^2 k^2 T/3|e|.\partial/\partial\epsilon(l_i A_i)/(l_i A_i)$$

and $\sigma_{x,i} = e^2/(12\pi^3 h).(l_i A_i)$.

It follows that

$$S_x = \Sigma_i \sigma_{x,i} S_{x,i}/\sigma_x \text{ ----- (24)}$$

If we now consider the effect on thermopower of various scattering processes we can show that the expression for thermopower S_x can be written as

$$S_x = \Sigma_i \rho_{x,i} S_{x,i}/\rho_x \text{ ----- (25)}$$

where S and ρ are the thermopower and resistivity associated with the various scattering mechanisms.

The proof is given below:

Equation (18) is

$$S_x = -\pi^2 k^2 T/3|e| \; [\partial/\partial\epsilon(\ln \sigma_x(\epsilon))]_{\epsilon=\epsilon_F} .$$

This is equivalent to

$$S_x = \pi^2 k^2 T/3|e| \; [\partial/\partial\epsilon(\ln \rho_x(\epsilon))]_{\epsilon=\epsilon_F} \quad \text{---- (26)}$$

If we now assume Matthiessen's rule is valid so that

$$\rho_x = \sum_j \rho_{x,j}, \text{ then we have}$$

$$S_x = \pi^2 k^2 T/3|e| \; [\partial/\partial\epsilon(\ln(\sum_j \rho_{x,j}))]_{\epsilon=\epsilon_F} \quad \text{---- (27)}$$

If we write $S_{x,j}$ as

$$S_{x,j} = \pi^2 k^2 T/3|e| \; [1/\rho_{x,j} \partial\rho_{x,j}/\partial\epsilon]_{\epsilon=\epsilon_F} \quad \text{---- (28)}$$

then it easily follows by combining equations (27) and (28) that

$$S_x = \sum_j \rho_{x,j} S_{x,j}/\rho$$

Any change in shape of the Fermi surface will affect the value of the thermopower as well as the sign of the thermopower. However the problem with thermopower is rather more complex than either electrical or thermal conductivities.

III. Sample Preparation and Characterisation

3.1 Sample Preparation

Samples were cut from the 2H-$TaSe_2$crystals such that the thermopower was measured perpendicular to the c-axis. Three batches of crystals were used for the measurements:

sample A - sample from DiSalvo (Bell Labs)

sample B - From batch 2-27-1 (grown previously in our laboratary)

sample C - From batch June 30/69 (grown previously in our laboratary)

The samples from batches A and B were cut from big crystals but for the sample C small crystals were used directly.

The resistance ratio R(296K)/R(4.2K) for these samples were measured using the 4 probe method. The samples were mounted on a sapphire plate using a thin film of epoxy between the sample and the sapphire plate. The four copper leads were connected to the sample using silver dag. The typical sample dimensions were approximately 0.1mm×1mm×10mm.

The resistance ratios were used as an indicator of the perfection of the sample. A higher resistance ratio sample is considered to have greater perfection since the scattering of electrons in the crystal by impurities, and crystal defects results in a higher resistivity at low temperatures.

3.2 Sample Charaterisation

The temperature vs resistivity curve for each sample was measured to give some indication of the sample perfection. The following resistance ratios were obtained from the data:

Sample	Resistance ratio R(296K)/R(4.2K)
A	182.1
B	37.1
C	22.7

Fig.3.1 Log plot for the temperature dependence of resistivity for 3 batches of 2H-$TaSe_2$ crystals.

(A) - batch A

(B) - batch B

(c) - batch C

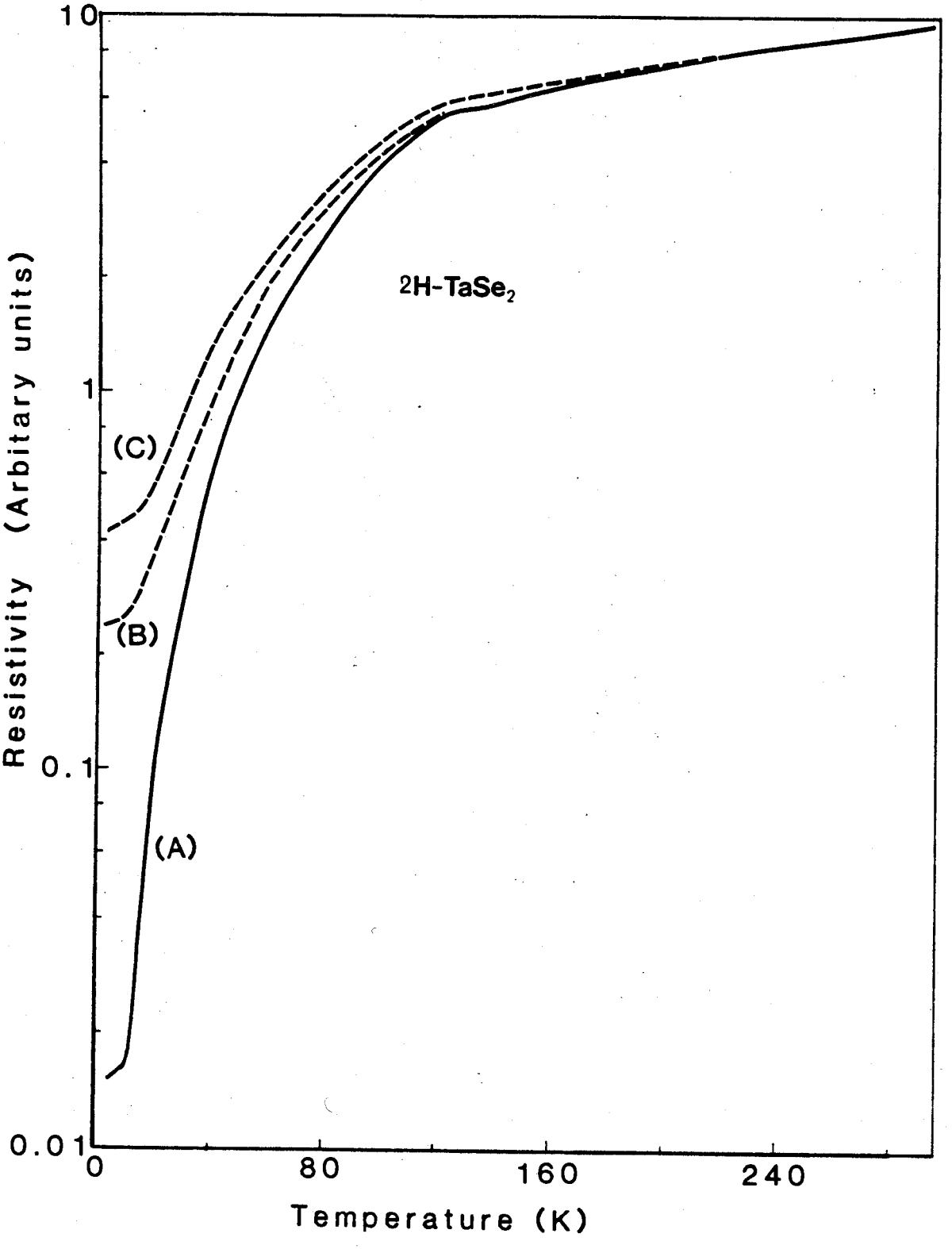
10
1
0.1
0.01
Resistivity (Arbitary units)
2H-TaSe2
(C)
(B)
(A)
0
80
160
240
Temperature (K)

FIG.3.1

3.3 Peaks at the Transition Temperature

The temperature vs resistivity curves in Fig.3.1 exhibit sharp changes in resistivity at the CDW transition temperature which occurs at 122K for batches A and B, and at 118.5K for batch C. According to the literature most of the 2H-$TaSe_2$ samples exhibit a transition at 122K. One should note that the sample C is less pure than samples A or B, as indicated by the residual resistance ratio.

The resistance and temperature scales were expanded for the samples A and B (Fig.3.2 (a),(b)). The percentage of peak height in comparison with resistivity at 122K was calculated to be 0.69% and 0.41% for A and B respectively. It seems that purer samples exhibit a higher resistance peak than the less pure samples.

3.4 Search for a Sliding CDW in 2H-$TaSe_2$

Thin samples of the order of 2000A in thickness were used in the search for non-ohmic effects in 2H-$TaSe_2$. It was shown(22) that in $NbSe_3$(a one-dimensional system) such effects were due to charge transport by a sliding charge density wave. The 2H-$TaSe_2$ samples were obtained by cleaving the 2H-$TaSe_2$ crystals and were mounted on a sapphire plate using an epoxy. Four copper leads connected to the sample using silver dag were used for the resistance measurement such that the resistance was measured across the thin part of the crystal. It was found that

there was no change in resistivity observed for electric fields up to 10V/cm. It was not possible to go beyond this electric field because of sample heating. These samples were in a cryostat which contained helium gas at very low pressure. It is possible to reduce the sample heating by immersing the sample into the liquid nitrogin(77K), but by analogy with the trichalcogenides the depinning of the CDW is expected to be easier close to the CDW transition temperature of 122K.

Fig.3.2 Temperature dependence of normalized resistivity $R(T)/R(T_0)$ near the CDW transition temperature T_0 = 122K for batches A and B 2H-$TaSe_2$ crystals. The curves on cooling and on warming are identical within the experimental results.

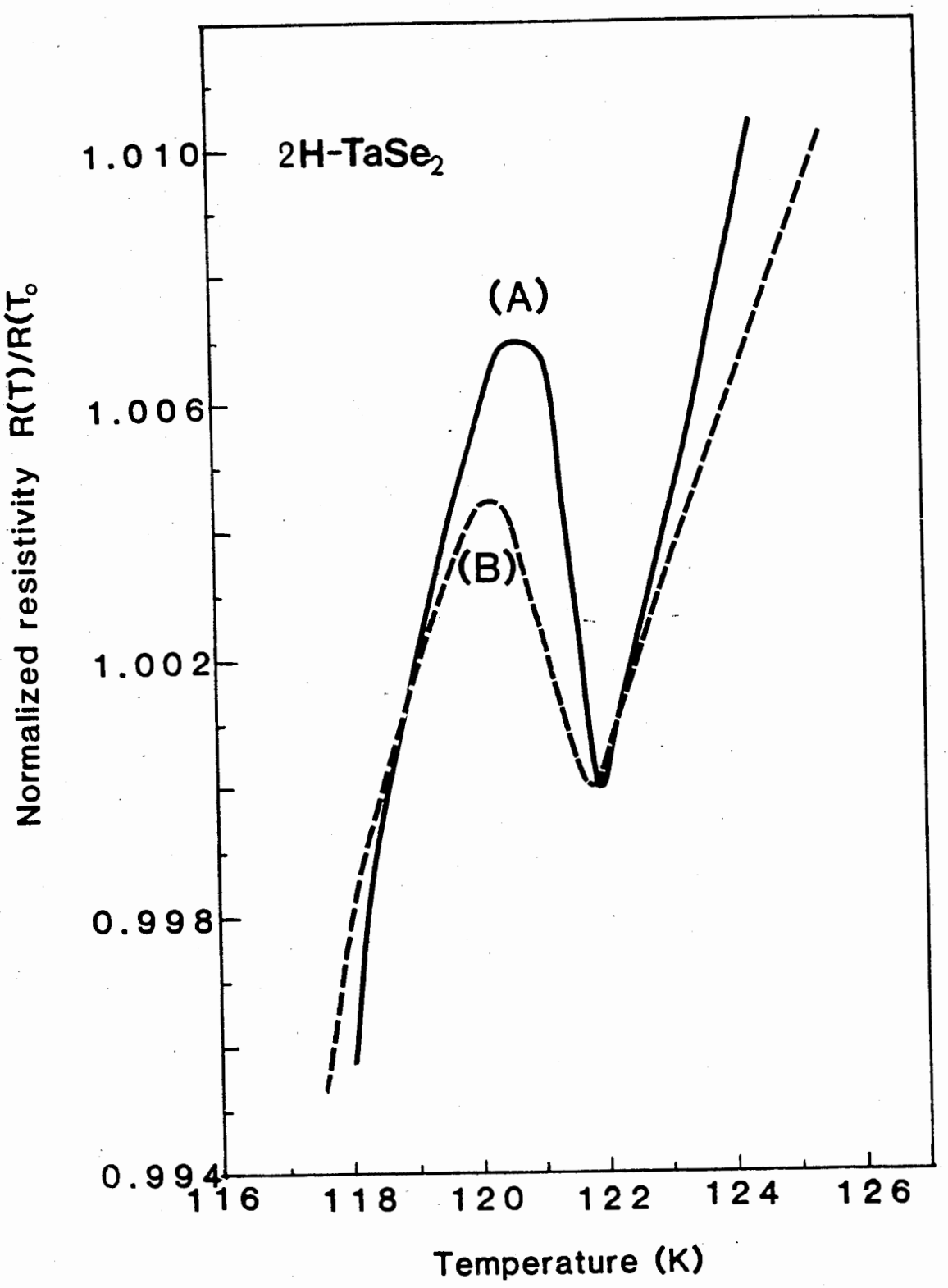
2H-TaSe2
(A)
(B)
1.010
1.006
1.002
0.998
0.994
116
118
120
122
124
126
Normalized resistivity R(T)/R(T0
Temperature (K)

FIG.3.2

IV. Thermoelectric Measurements

4.1 General Considerations

In measuring the themoelectric properties of metals and alloys there is almost always recourse to the construction of thermocouple arrangements so that the Seebeck E.M.F. is measured when one junction is raised in temperature relative to other. In order to obtain the thermopower S of a thermocouple incoporating the sample under test, one of two procedures is commonly adopted.

4.1.1 Integral Method

In this method a constant temperature bath is used which holds one junction at a known temperature (this may be boiling helium or nitrogen, an ice bath or an electronically controlled isothermal chamber), the other junction is raised in temperature and the total E.M.F. measured over the temperature range of interest. To obtain S it is then necessary to differentiate the V versus T curve.

4.1.2 Incremental Method or Differential Method

This scheme has been given by Crisp,Henry and Schroeder(24). In this method, the thermopower can be obtained directly by raising both junctions to the required temperature and then further increasing one junction by a small increment ΔT, say up to 1K, and measuring the small E.M.F. ΔV so created. The thermopower at the temperature $T+\Delta T/2$ is then $S \simeq \Delta V/\&T$

Both methods are capable of giving accurate thermopowers, the first however requires more data processing but the second requires at best three measurements, i.e. T, ΔT, ΔV, whereas only T and V are required in the former case. In some cases it is only possible to utililze the second differential method, particularly in the study of ordering processes and phase changes where the whole sample must be in a virtually isothermal environment.

In practice the E.M.F. as indicated by a sensitive voltmeter will inevitably include some steady thermal E.M.F's generated in the leads to the instruments. These can arise, for example, from lack of homogeneity of the conductors and can lead to serious errors in the differential method where the required thermal E.M.F's are small. To eliminate these spurious E M F's in ΔV and ΔT (assuming T is measured by a thermocouple), it is usual to take at least two values of ΔT and then S is the slope of the ΔV vs ΔT plot. Such plots can be displayed directly on an X-Y recorder. These plots rarely pass through the origin indicating that spurious E.M.F.'s are nearly always present.

4.2 Experimental Apparatus

The measurments described here use the incremental(or differential) method to measure the thermoelectric power. Fig.4.1(a) shows the sample holder in the cryostat used for this purpose. It contains two copper blocks which were separated by an insulating material(Bakelite).

Au+0.07%Fe vs chromel thermocouples were used to measure the temperature difference between the blocks and the absolute temperature of the upper block. In measuring the absoulute temperature, an ice bath was used for the reference junction. This thermocouple has a sensitivity of 20 μV/K in the 60K to 120K temperature region which is the main temperature region of interest in this work.

The distance between the copper blocks was of the order of 3mm. The sample was mounted between the copper blocks using silver dag, and copper leads, connected to the sample by silver dag were used to measure the thermoelectric potential across the sample (Fig.4.1(b)). Typical sample dimensions were approximately 5mm×0.5mm×50 m.

A small amount of helium gas (pressure of the order of 2psi at room temperature) was used as the exchange gas in the cryostat. Experiments were also done without the exchange gas, and gave the same results. The use of the exchange gas greatly shortered the time required to cool the cryostat. Liquid nitrogen was used to cool the cryostat down to 77K. Temperatures

down to about 60K were achieved by pumping on the liquid nitrogen. For measurements below 60K liquid helium was used as the coolant.

Three heating coils were used to control the overall temperature as well as the temperature difference between the blocks(Fig.4.1(b)). Heating coils H_1 and H_2 were used to control the overall temperature and heating coils H_2 and H_3 were used to control the temperature difference between the copper blocks. The temperature of the upper copper block could be held constant within 0.2K during the temperature scan of the lower copper block.

Fig.4.1 (a) The system used to measure thermopower. The sample holder in the cryostat.

(b) The sample holder of the cryostat showing the heating coils.

(c) A typical 2H-$TaSe_2$ crystal cut (cross-hatched area) which was used for the measurements for the batches A and B crystals. The area of the crystal shown here is normal to the C-axix.

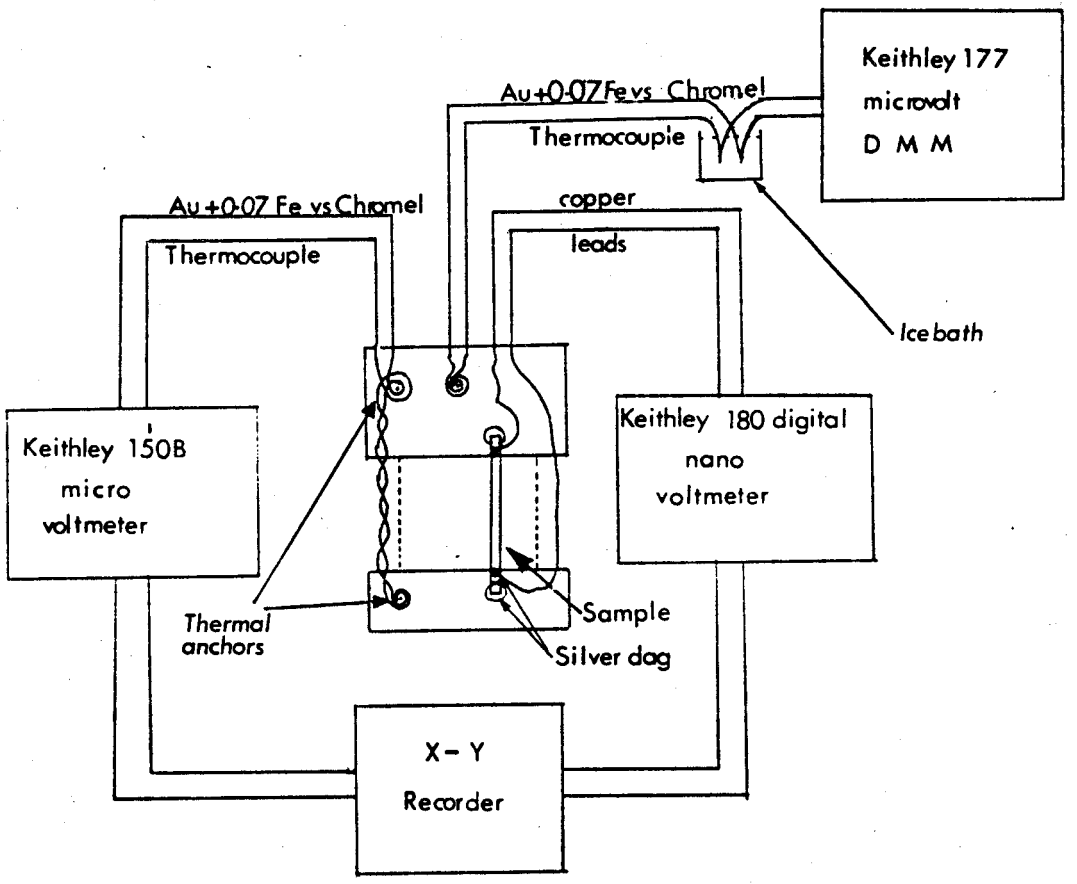

(a)

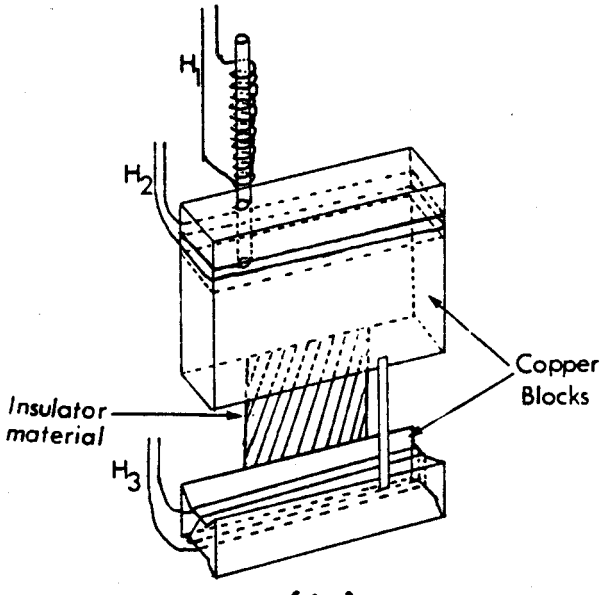

(b)

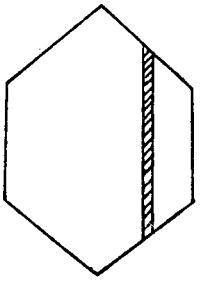

2H-$TaSe_2$ Crystal

(c)

FIG.4.1

4.3 Experimental Method

The thermocouple which measured the temperature difference was connected to a microvoltmeter with a sensitivity of 1 μV and the analog output terminals of the microvoltmeter were connected to the X-terminals of an X-Y recorder. The thermoelectric potential across the sample was measured using a nanovoltmeter and the analog output of this meter was connected to the Y-terminals of the X-Y recorder.

At a particular temperature of the upper block the temperature difference between the blocks was changed from +0.5K to -0.5K. The thermopower was determined from the gradient of a graph of sample voltage against temperature difference which was plotted on the X-Y recorder (Fig4.2(a)). By subtracting the absolute thermopower of copper (Fig.4.2(b))(26) from the value calculated above the absolute thermopower of 2H-$TaSe_2$ was determined. The measured values of the thermopower for 2H-$TaSe_2$ are estimated to be accurate within 0.05 μV/K.

Fig.4.2 Typical plots from x-y recorder traces showing thermoelectric potential vs sample temperature difference for 4 different temperatures.

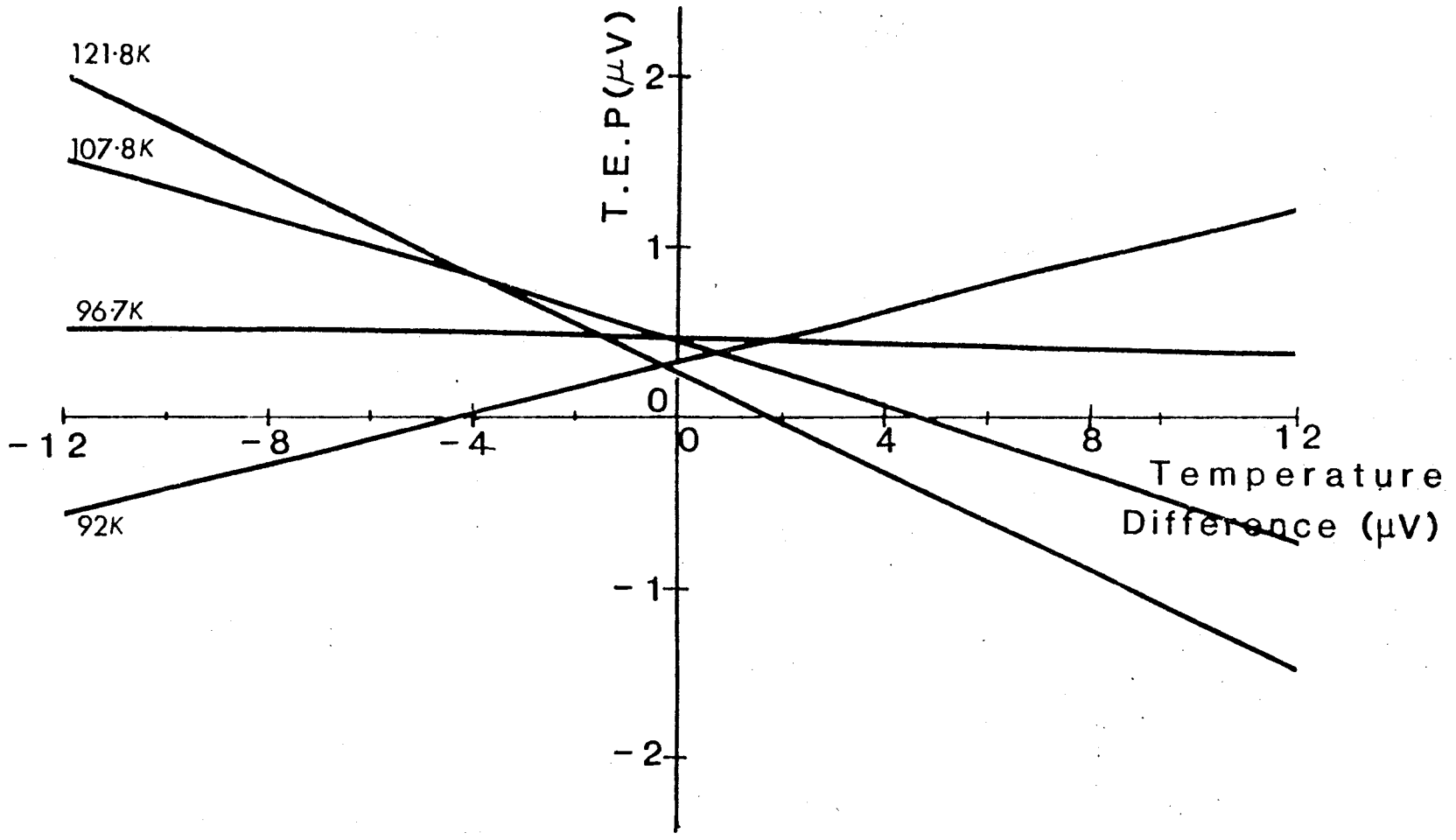
121·8K
107·8K
96·7K
92K
T.E.P (μV)
2
1
0
-1
-2
-12
-8
-4
0
4
8
12
Temperature
Difference (μV)

FIG.4.2(a)

Fig.4.2(b) Temperature dependence of thermopower for Copper(After Macdonald (26)).

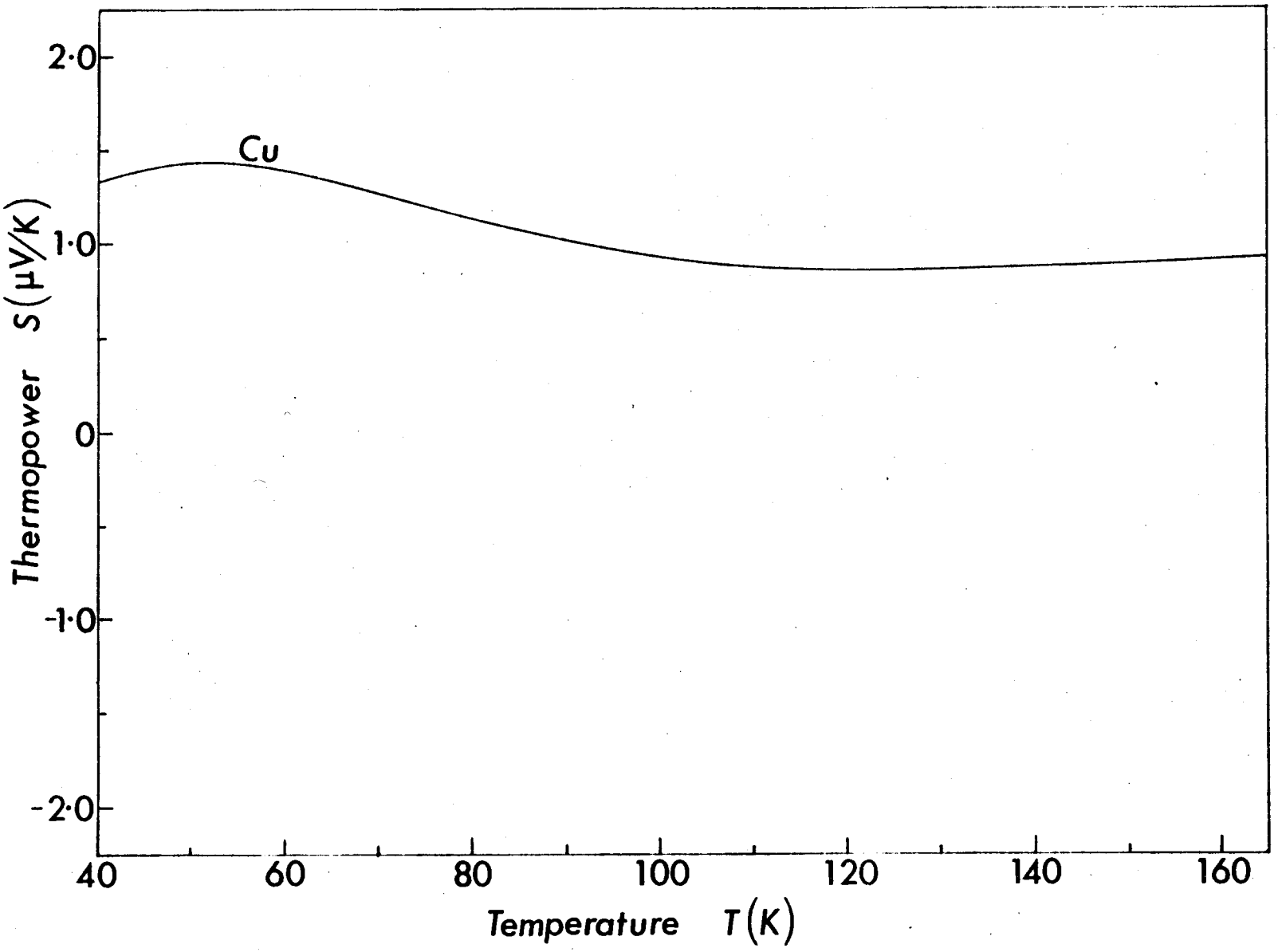
2·0
1·0
0
-1·0
-2·0
Cu
Thermopower S(μV/K)
40
60
80
100
120
140
160
Temperature T(K)

FIG·4·2(b)

4.4 Results

The thermopower of 2H-$TaSe_2$ was measured over the temperature range 60K to 140K for three batches of crystals. One sample from each batch A and C and two samples from two different batch B crystals were studied. Thermopower results obtained for the two samples from two different batch B crystals were quite consistent. At room temperature the thermopower S for the batch B crystal is -2.0 μV/K. The CDW transition was observed at 122K for batches A and B crystals and at 118.5K for a batch C crystal(Fig.4.3, 4.4, 4.5). The thermopower varies linearly with temperature above the CDW transition temperature and a sharp drop occurs at the transition temperature for all three batches of crystals. The thermopower S at 122K is +2.3 μV/K for the batch A crystal. The value of S is slightly smaller at this temperature for the B and C samples as shown in Figs.4.4 and 4.5. Above the transition temperature (122K) the slope of the curve for the batch A crystal is 28% lower than for the batch B and C crystals.

4.4.1 Cooldown below the transition temperature

Below the transition temperature the thermopower decreases with decreasing temperature and it changes sign at 105K for the batch A crystal. The thermopower changes sign at 92K and 93K for the batches B and C respectively. For the batch A crystal a

small change of slope is observed at 105K. This is not present in the batches B and C.

For the batch A crystal another sharp change in slope occurs at 87K at a value of -1.7 μV/K. Below this temperature the curve is flat down to 75K and then slowly starts to decrease negatively. This transition at 87K is not clearly evident for the batches B and C and rounded minima in the thermopower are seen at lower temperatures for these samples.

Fig.4.3 Temperature dependence of thermopower in 2H-$TaSe_2$ for the batch A crystal is shown for cooling and warming. Open circles represent the cooling curve and closed circles represent the warming curve.

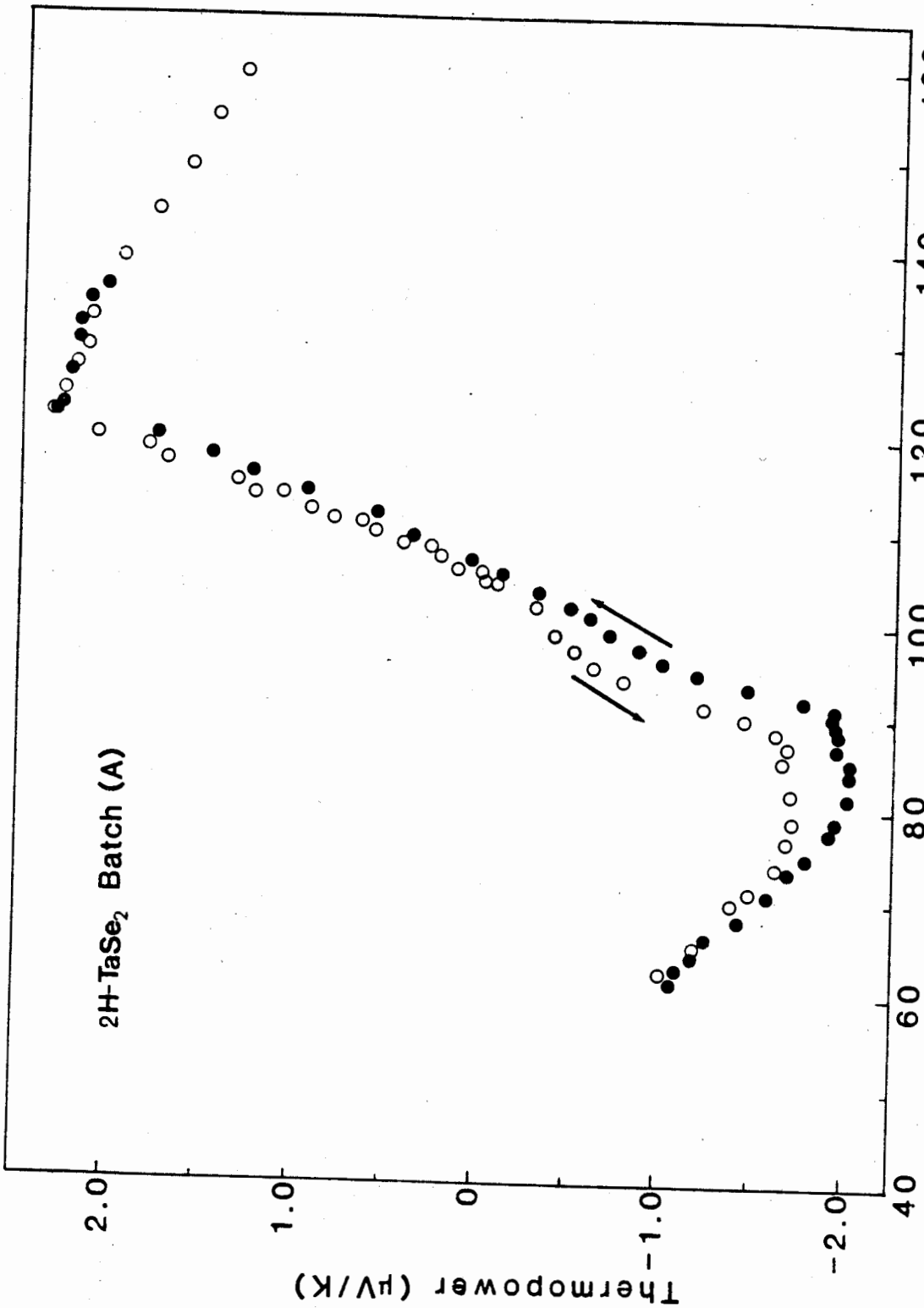
2H-TaSe2 Batch (A)
Thermopower (μV/K)
Temperature (K)
2.0
1.0
0
-1.0
-2.0
40
60
80
100
120
140
160

FIG.4.3

Fig.4.4 Temperature dependence of thermopower in 2H-$TaSe_2$ for a batch B crystal is shown for cooling and warming.

+ - cooling

o - warming

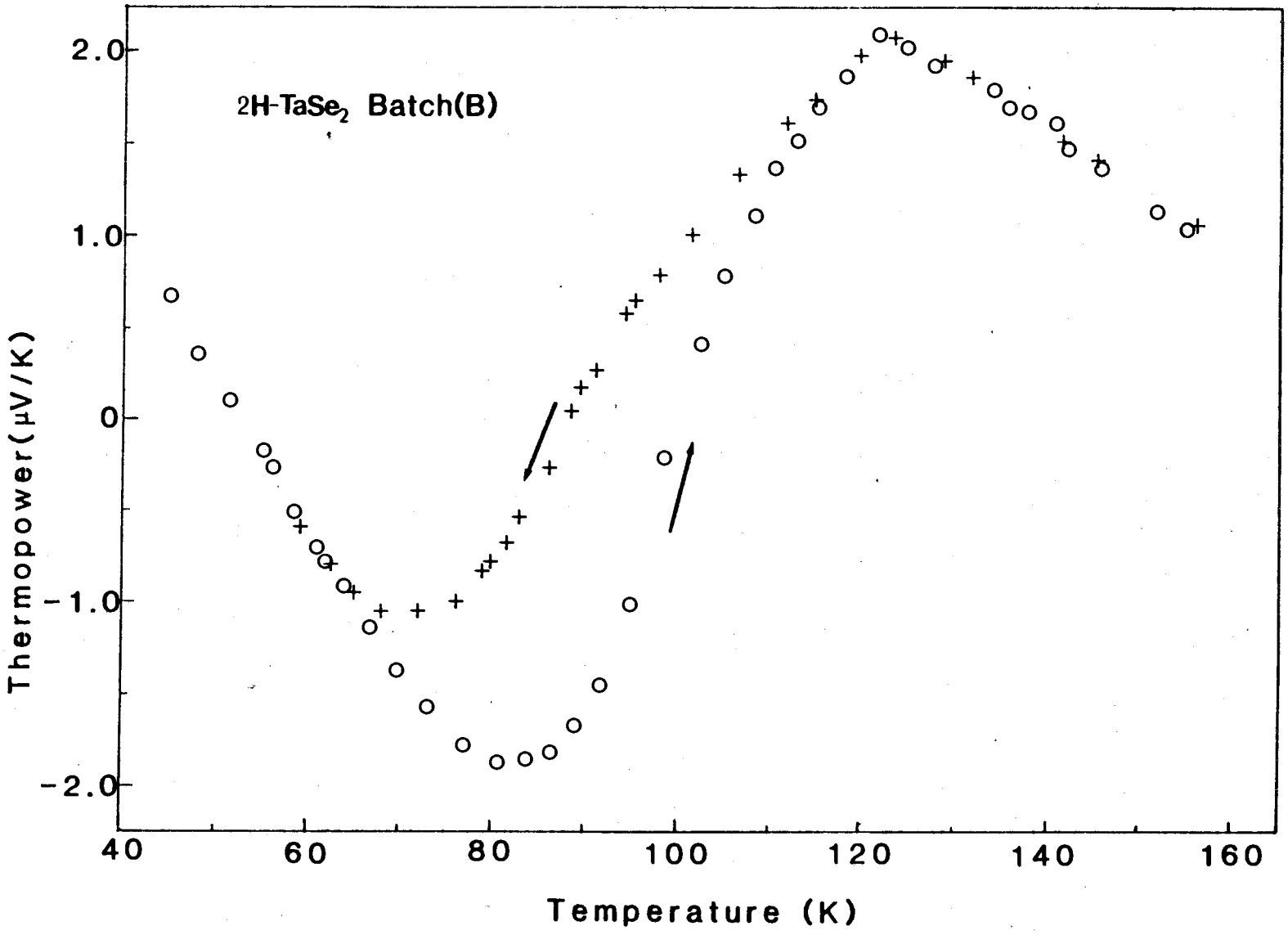
2H-TaSe2 Batch(B)
Thermopower(μV/K)
2.0
1.0
0
-1.0
-2.0
40
60
80
100
120
140
160
Temperature (K)

FIG.4.4

Fig.4.5 Temperature dependence of thermopower in 2H-$TaSe_2$ for the batch C crystal is shown for cooling and warming. Open circles represent the cooling curve circles represent the warming curve.

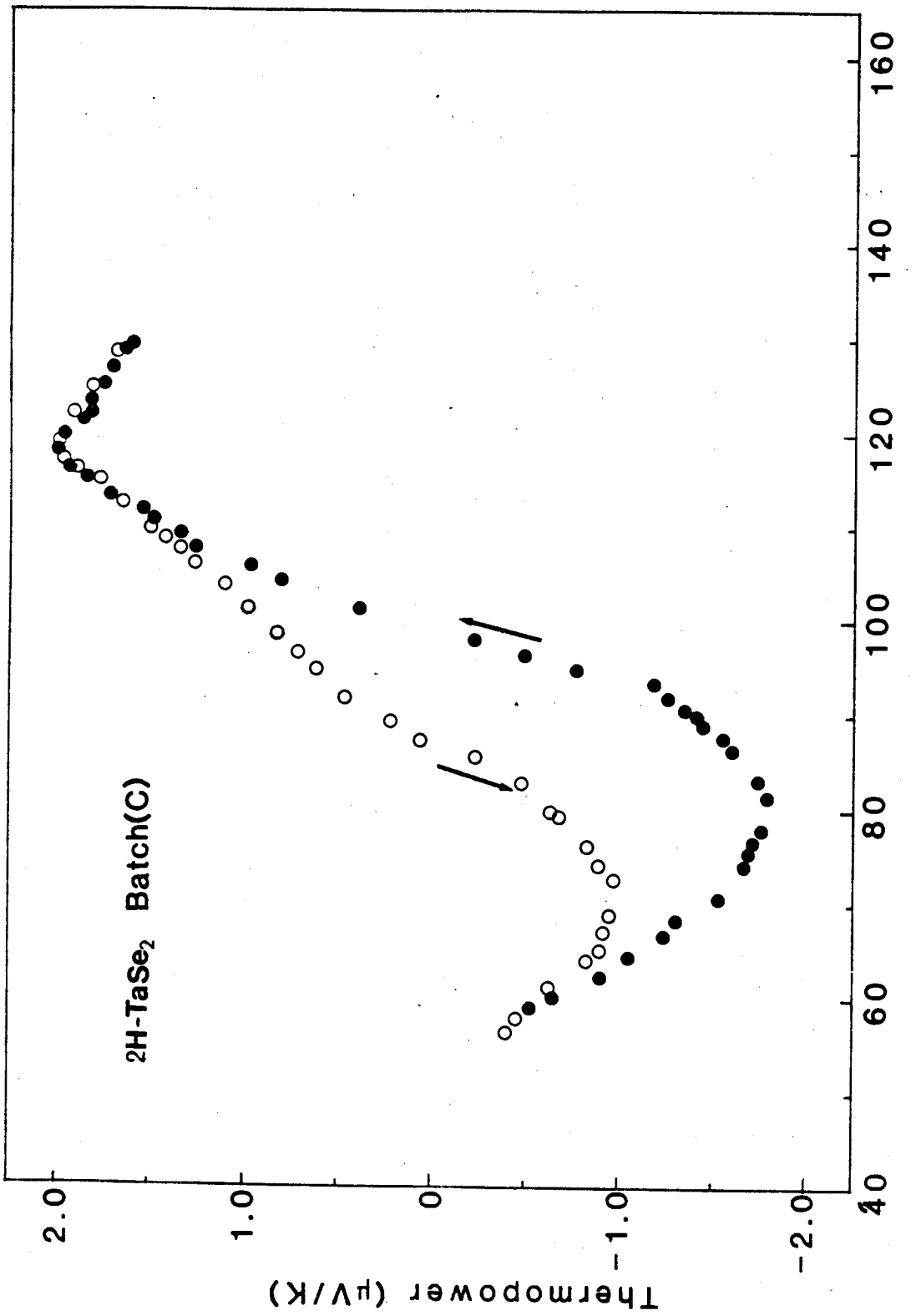
2H-TaSe2 Batch(C)
Thermopower (μV/K)
Temperature (K)
2.0
1.0
0
-1.0
-2.0
40
60
80
100
120
140
160

FIG.4.5

4.4.2 Warmup

On warming from 60K the thermopower increases negatively, following the cooldown, up to about 65K. It still increases negatively up to 75K and then the increase is less rapid. The minimum value of the thermopower for a batch A crystal is -2.0 μV/K at 85K. A sharp change occurs at 92K for batch A and the thermopower decreases negatively with increasing temperature and changes sign at 106.5K. It is evident from the warmup and cooldown curves that there is a significant hysteresis from 65K to 105K and a comparatively small hysteresis from 105K to 122K.

Samples B and C exhibit a much larger hysteresis than the batch A crystal. The warmup curves are more similar to the batch A crystal than the cooldown curves and the minima is observed at about 80K, at values of -1.75 μV/K and -1.5 μV/K for the batches B and C respectively. At about 92K the negative thermopower decreases more rapidly and changes sign at about 100K.

The large hysteresis exhibited in batches B and C was studied in some detail and is shown in Fig.4.6a and 4.6b. Note that there is no hysteresis observed when a sample is warmed from 65K to 87K and cooled down again, as indicated in Fig.4.6b for the batch B sample, but a sample warmed from 65K to 95K is observed to exhibit some hysteresis, as indicated in Fig.4.6b for the batch C sample.

Fig.4.6a The observed thermopower for 2H-$TaSe_2$ batch B crystal when warming and cooling from different initial temperatures.

× - cooling from above the transition temperature 122K

o - warming after cooing down to below 95K.

◁ - warming after cooling down to 77K.

□ - warming after cooling down to 70K.

⊙ - warming after cooling down to 65K.

+ - cooling after warming from below 65K to 99K.

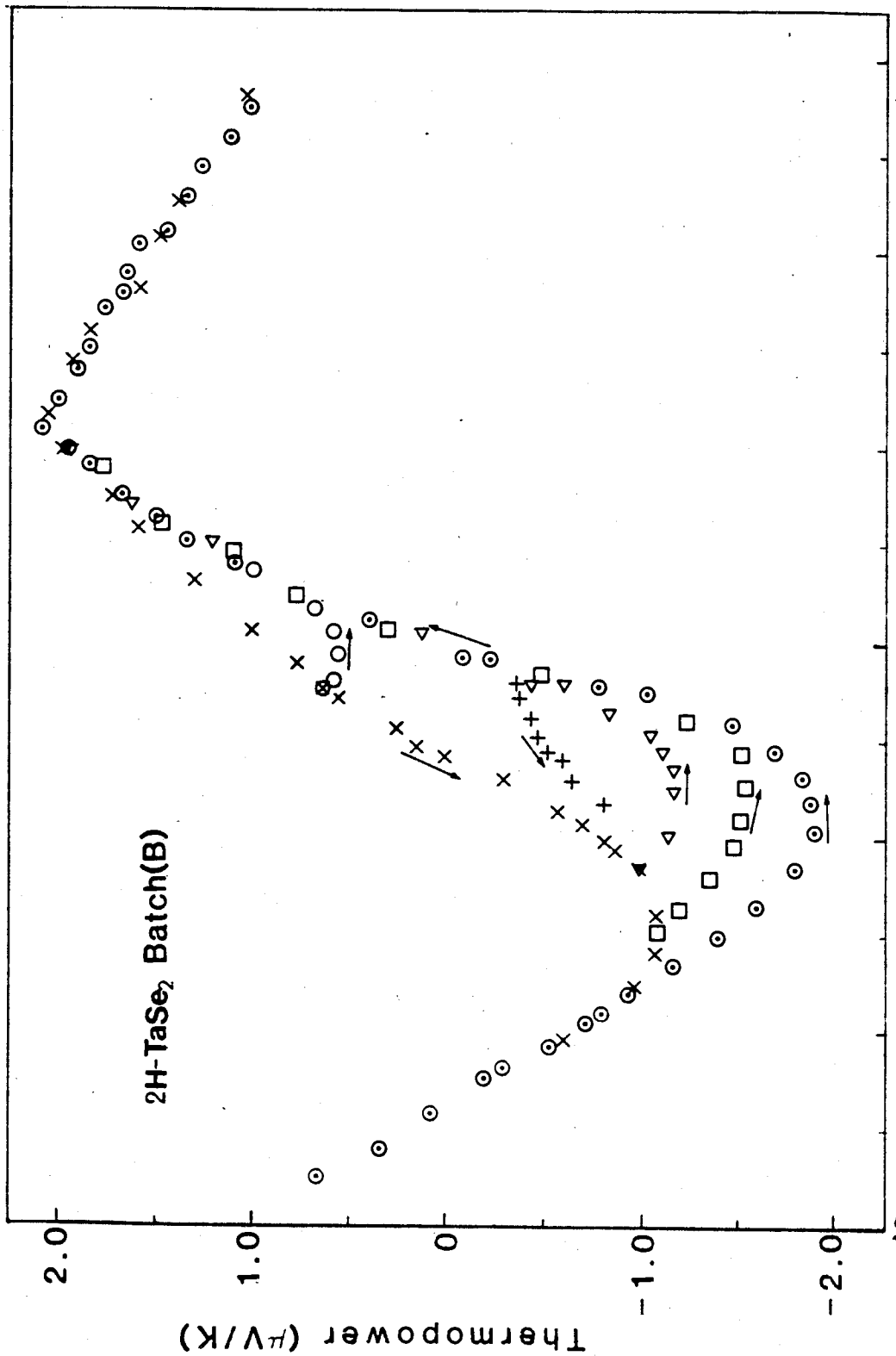
2H-TaSe2 Batch(B)
Thermopower (μV/K)
Temperature (K)
2.0
1.0
0
-1.0
-2.0
40
60
80
100
120
140
160

FIG.4.6a

Fig.4.6b The observed thermopower for 2H-$TaSe_2$ batch B and C crystals when warming and cooling from different initial temperatures.

Δ - cooling from above 122K in batches B and C.

o - warming from below 65Kin batches B and C.

Δ - Cooling after warming from below 65K to 88K in batch B.

Δ - Cooling after warming from below 65K to 95K in batch C.

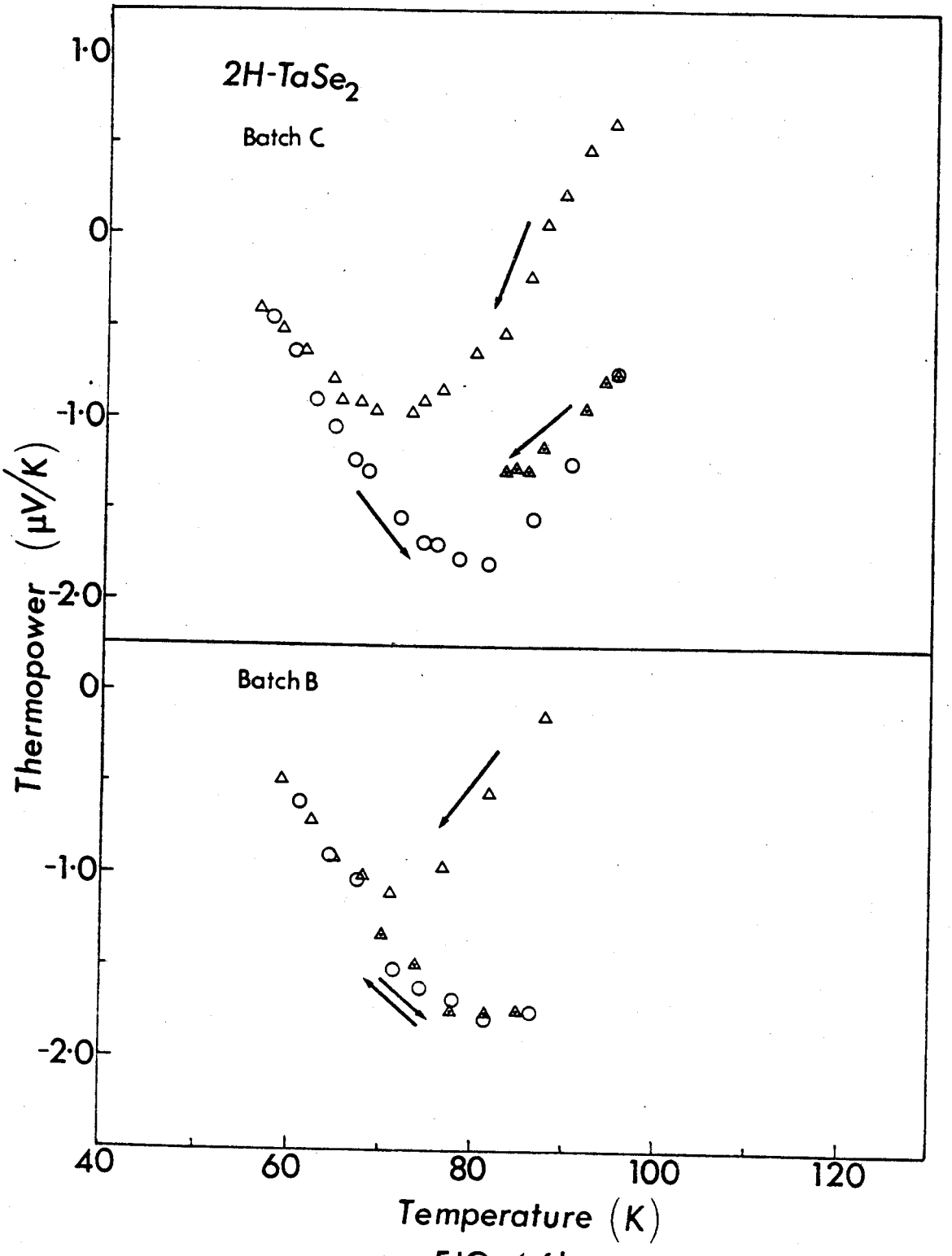
2H-TaSe2
Batch C
Batch B
1·0
0
-1·0
-2·0
0
-1·0
-2·0
Thermopower (μV/K)
40
60
80
100
120
Temperature (K)

FIG·4.6b

4.5 Hysteresis in Thermopower

The hysteresis in thermopower between cooling and warming was plotted as a function of temperature is shown in Figs.4.7, 4.8 and 4.9 for batches A,B and C crystals respectively. All the curves exhibit a peak near 90K and vary smoothly above and below 90K except the batch A crystal. The batch A crystal exhibits a peak at about 90K as well as a dip at about 103K. This peak at 90K is similar to the peak exhibited in the hysteresis in resistivity vs temperature curve (Fig.1.4(b)).

Fig 4.7 Temperature dependence of hysteresis in thermopower is plotted for batch A 2H-$TaSe_2$ crystal. The absolute value of the difference in thermopower on cooling and warming is taken as the hysteresis.

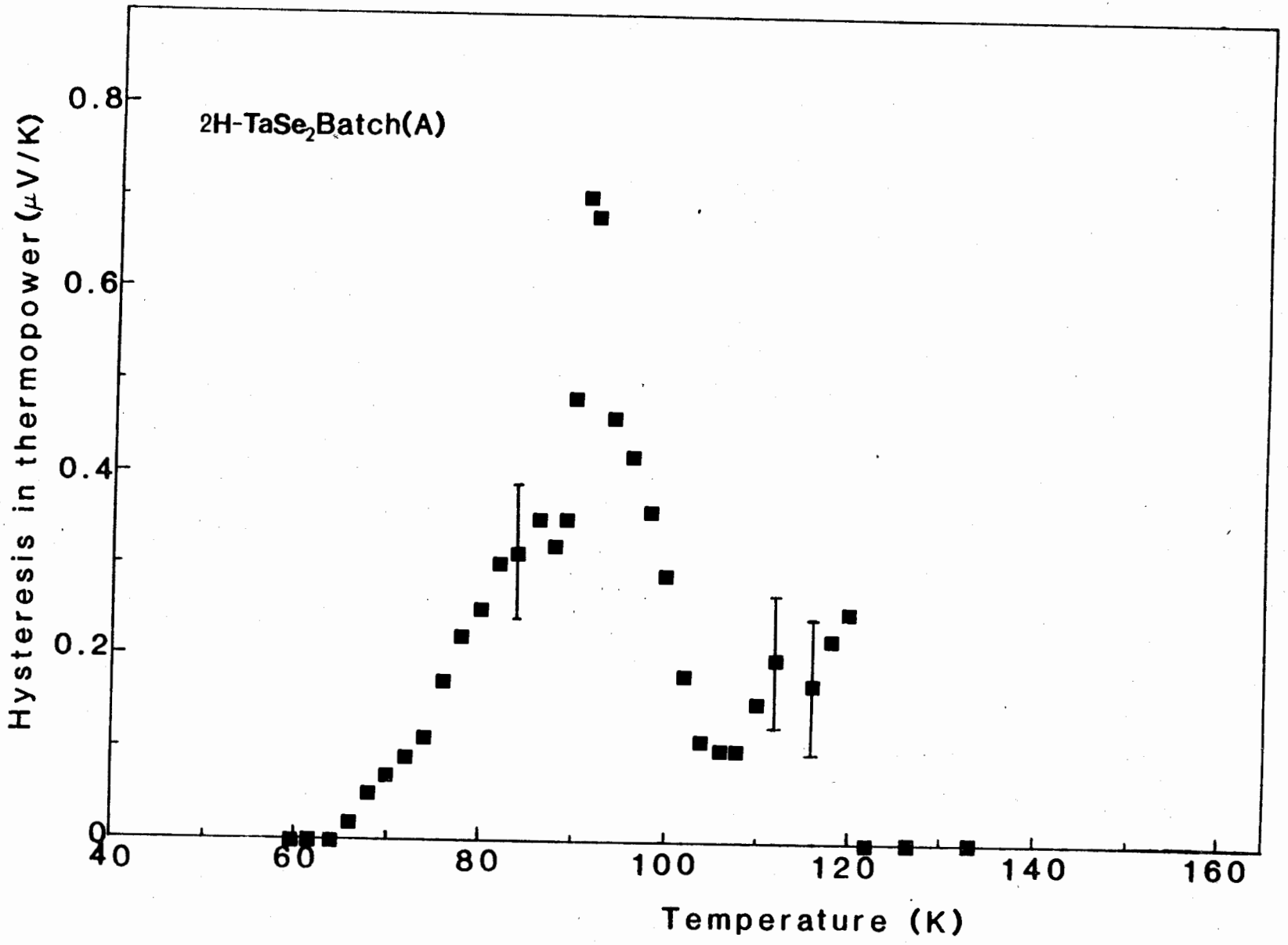
2H-TaSe2Batch(A)
Hysteresis in thermopower (μV/K)
0.8
0.6
0.4
0.2
0
40
60
80
100
120
140
160
Temperature (K)

FIG.4.7

Fig 4.8 Temperature dependence of hysteresis in thermopower is plotted for batch B 2H-$TaSe_2$ crystal. The absolute value of the difference in thermopower on cooling and warming is taken as the hysteresis.

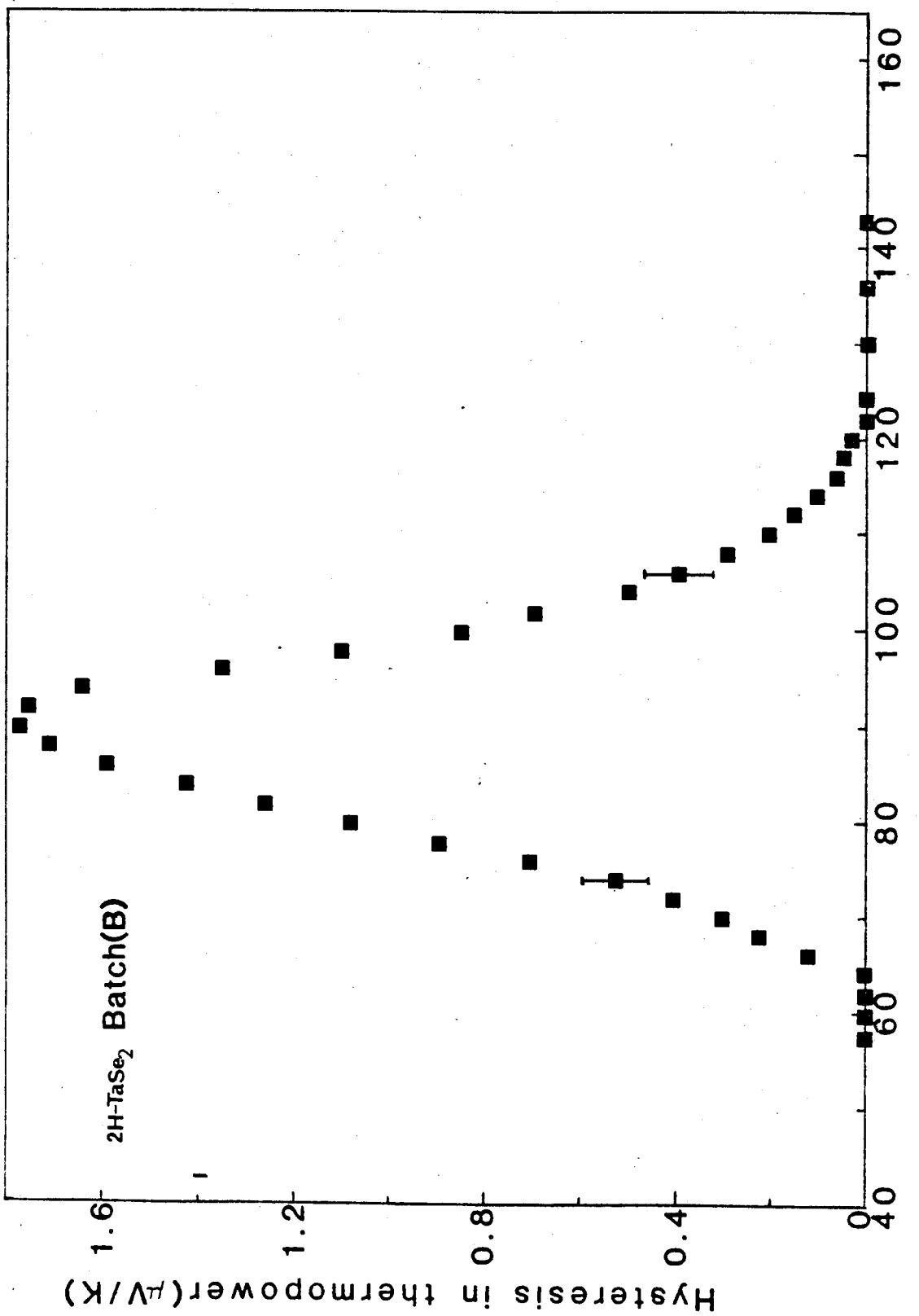
Hysteresis in thermopower(μV/K)
1.6
1.2
0.8
0.4
0
40
60
80
100
120
140
160
Temperature (K)
2H-TaSe2 Batch(B)

FIG.4.8

Fig 4.9 Temperature dependence of hysteresis in thermopower is plotted for batch C 2H-$TaSe_2$ crystal. The absolute value of the difference in thermopower on cooling and warming is taken as the hysteresis.

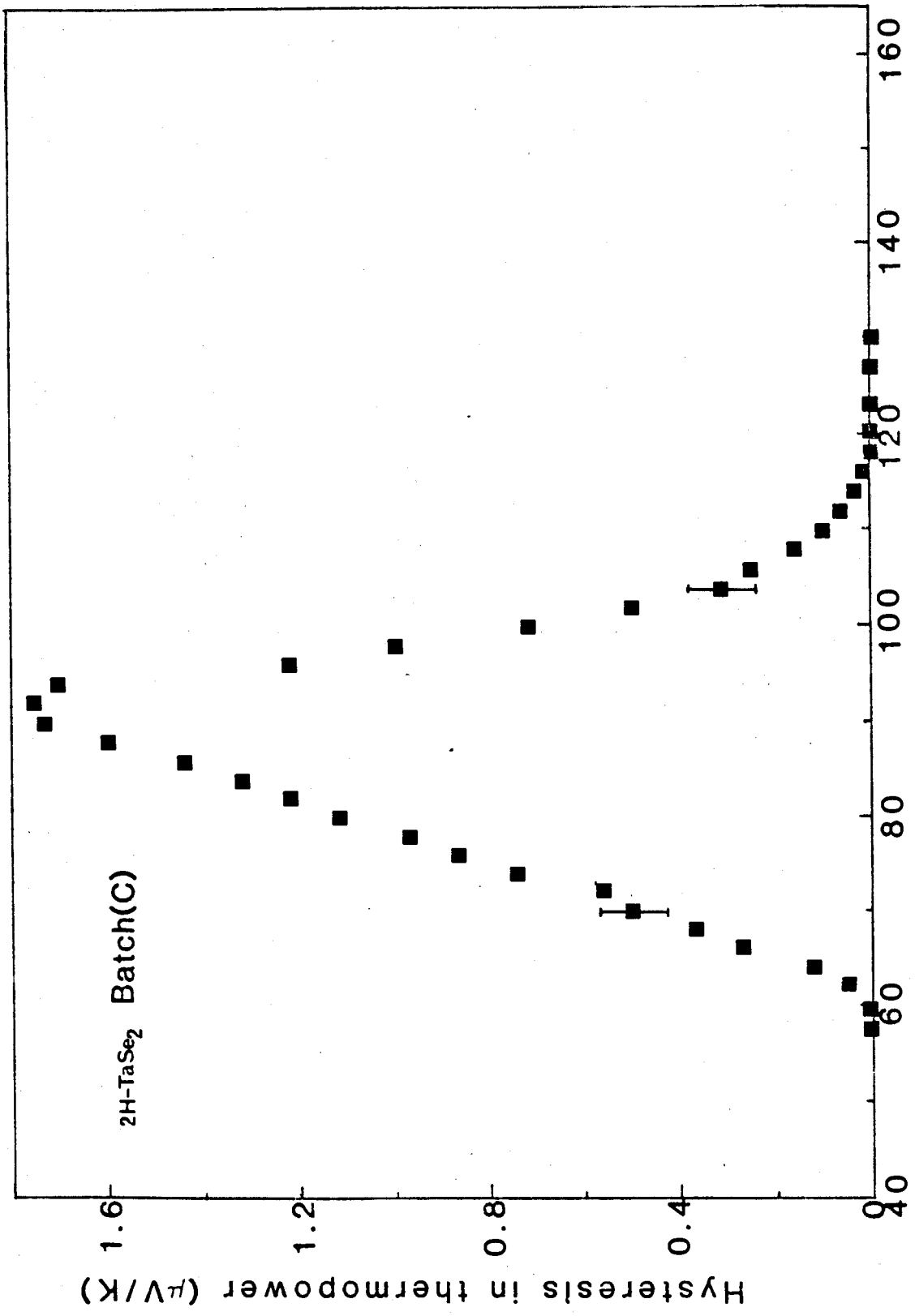
Hysteresis in thermopower (μV/K)
1.6
1.2
0.8
0.4
0
40
60
80
100
120
140
160
Temperature (K)
2H-TaSe2 Batch(C)

FIG.4.9

V. Discussion

The temperature dependent thermopower measurements presented here on 2H-$TaSe_2$ are new results. At room temperature the thermopower is negative and the Hall coefficient is positive. This conflict in sign indicates both positive and negative carriers involved in the transport. In the region near T_0(122K) the Hall coefficient and the thermopower are positive. This indicates the predominence of holes over electrons in this region. With the onset of the charge density wave (below 122K) both the thermopower and the Hall coefficient start to decrease positively and change sign. The decrease in positive thermopower and positive Hall coefficient means more electron participation in transport over holes(29), that is the creation of electron surfaces and/or the destruction of hole surfaces changes the sign of the first (Fermi surface dependent) term in equation (22).

The hysteresis in thermopower vs temperature curves (Fig.4.7, 4.8 and 4.9) exhibit peaks at about 90K for all 3 batches of crystals which are similar to the hysteresis in resistivity vs temperature curve (Fig.1.4(b)). The behavior of the hysteresis in thermopower between 90K and 122K is similar to the hysteresis in resistivity to some extent only in the batch A crystal. We note that the batch A cryatal has the higher resistance ratio. The hysteresis in the resitivity curve is not given below 87K but is rapidly dropping.

The X-ray and neutron diffraction results do not show any structural changes below 85K. The high resolution X-ray diffraction results in Fig.1.6(a) exhibits a hysteresis down to about 85K but show no changes or hysteresis below 85K. The X-ray work shows the incommensurate-commensurate transition at 85K on cooling and at 93K in warming. Sharp changes in slope of the thermopower close to these temperatures is present in batch A crystals but not in other batches of crystals. The hysteresis exhibited between 122K and 90K in the X-ray results is reasonably consistent with the thermopower hysteresis, but the hysteresis exhibited in the thermopower below 90K is inconsistent with the absence of hysteresis in the X-ray data.

According to the electron microscopy results reported in sec.1.5 on cooling, CDW domains became apparent at 80K and these domains combined into large domains with decreasing temperature. No changes in domain structure were seen below 65K. On warming no changes in domain structure were seen up to 80K.

Fig.5.1 Schematic diagrams of CDW domains for 2H-$TaSe_2$ at different temperatures on cooling and warming, based on electron microscopy studies between 65K and 85K.

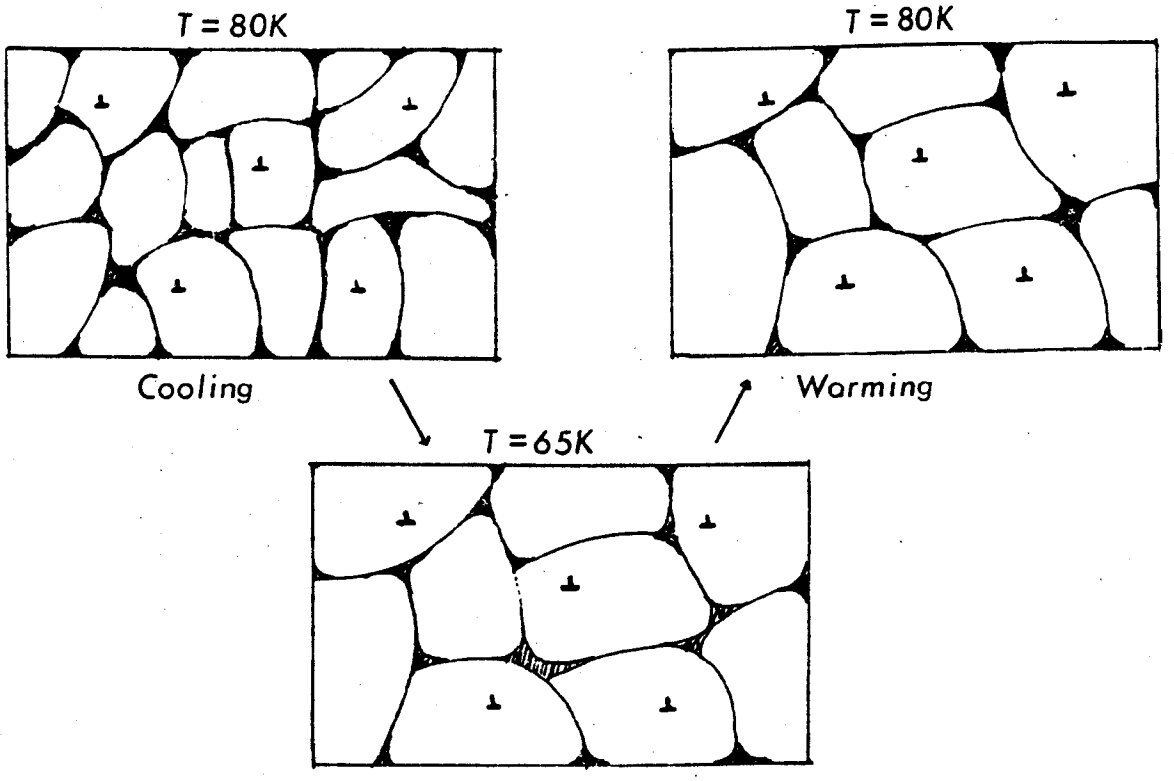

FIG. 5.1

Now the CDW domain walls can be expected to cause scattering of the electrons, so that larger domains will cause less scattering than smaller domains leading to a longer mean free path for larger domains.

The effect of two or more types of scattering on the thermopower of a given group of electrons is given by

$$S_x = \sum_j \rho_{x,j} S_{x,j} / \Sigma \rho_{x,j} \text{---- (25)}$$

where

$\rho_{x,j}$- Resistivity due to one type of scattering.

$S_{x,j}$- Thermopower for one type of scattering.

In our case we have two types of scattering, defect scattering and domain wall scattering (ignoring phonon scattering (see page 71)).

Then $S = (\rho_1 S_1 + \rho_2 S_2)/(\rho_1 + \rho_2)$ --- (29)

and $\rho = \rho_1 + \rho_2$ --- (30)

where S_1 and ρ_1 represents thermopower and resistivity due to defect scattering.

S_2 and ρ_2 represents thermopower and resistivity due to domain wall scattering.

For a particular crystal the thermopower S_1 and resistivity ρ_1 due to impurity scattering should be independent of domain size variation. Similarly S_2 and ρ_2 should be independent of the impurity scattering.

The magnitude of the thermopower hysteresis exhibited between 122K and 65K was calculated at 85K for the batch A crystal by extrapolating the the normal state (above 122K) curve down to 85K and calculating the percentage of hysteresis with respect to the normal state. The calculated magnitude of the thermopower hysteresis at 85K is 7.5%. In comparison with the hysteresis in resistivity (0.6%) the thermopower hysteresis is much larger. This can be discussed in terms of equations (29) and (30). If ρ_1 very much greater than ρ_2, any change in ρ_2 due to domain size variation will have a small effect on ρ. This requires that the change in S_2 due to domain size variation be quite large so that it will have a significant effect on the thermopower S.

In Fig.1.6 the hysteresis in resistivity is approaching zero at 87K. However since there is some hysteresis in thermopower exhibited between 87K and 65K, a small hysteresis in resistivity still can be expected in this temperature range.

If we can assume that the thermopower which is attributed to domain boundary scattering can be discussed generally in terms of equation (22) in sec.2 which applies to a spherical Fermi surface then we can use

$$S = -\pi^2 k^2 T/3|e| \; [1/A.\partial A/\partial \epsilon + 1/l.\partial l/\partial \epsilon]_{\epsilon=\epsilon_F} \quad \text{--- (22)}$$

where A is the area of the Fermi surface,

l is the mean free path

ϵ is the electron energy.

Since there are no structural changes below 85K according to the X-ray data it is reasonable assume that the term $1/A.\partial A/\partial \epsilon$ is a constant below 85K. So the domain wall scattering can be associated with the term $1/l.\partial l/\partial \epsilon$ where l is the mean free path. For small domains the mean free path would be smaller due to more domain wall scattering. But the thermopower results indicate that the larger domains lead to a high negative thermopower. This means a longer mean free path leads to a higher negative thermopower. This seems to indicate that the term $\partial l/\partial \epsilon$ is negative for CDW domain boundary scattering ($\partial l/\partial \epsilon$ is generally positive in most systems).

In crystals with high defect density the domain sizes can be expected to be smaller than for low defect density crystals. But crystals with a low resistance ratio exhibit a large hysteresis, i.e. high defect density crystals exhibit a larger hysteresis than the low defect density crystals. This indicates that the difference in domain size on cooling and warming could be larger in high defect density crystals than the low defect density crystals. The decrease in maximum negative thermopower

for high defect density crystals (as seen when Figs.4.3 and 4.5 are compared) seems to be consistent with the view that larger domains lead to higher negative thermopower.

The expression derived for thermopower in Sec.2 is only the contribution by the diffusion thermopower. In addition to this term a contribution from the phonon drag thermopower will also present(31). (The Debye temperature θ_D for 2H-$TaSe_2$ is 140K(27)). The phonon drag thermopower typically peaks in the temperature range between θ_D /10 and θ_D/5 and decays as T apporaches the Debye temperature(28). So we can assume that in our temperature range of interest 65K to 122K the phonon drag contribution would be relatively constant or negligible.

CONCLUSION

The thermopower was measured for 3 batches of 2H-$TaSe_2$ crystals between the temperature range 40K to 160K. It is positive above and close to the CDW transition temperature at 122K. On cooling, the thermopower decreases positively below the transition temperature and changes sign at about 105K for crystals with the least defects and changes sign at lower temperatures for crystals with a higher defect concentration. A change in slope is exhibited close to 90K in the crystal with the least defects but this is not observed in higher defect crystals. These high defect crystals exhibit rounded maxima in negative thermopower at about 70K and on warming the thermopower exhibits a large hysteresis between 65K and 110K and a relatively small hysteresis between 110K and 122K.

The thermopower hysteresis was compared with that found from X-ray experiments. The hysteresis in the X-ray results was found to be reasonably consistent with that in the thermopower between 122K and 85K. The hysteresis exhibited in the thermopower below 85k is not present in the X-ray results. The hysteresis in the thermopower vs temperature curve was plotted for all the samples and the peak exhibited at about 90K in all curves is consistent with the peak exhibited in the hysteresis in the resistivity vs temperature curve, but the hysteresis exhibited below 87K in the thermopower is not present in the resistivity.

The hysteresis in thermopwer below 85K is reasonably consistent with the domain size variation observed by dark field electron microscopy. The hysteresis was explained in terms of scattering of electrons by domain walls which leads to a change in mean free path with domain size. The change in mean free path was also discussed using the expression for thermopower derived from the Boltzmann transport equation.

BIBLOGRAPHY

(1) Wilson.J.A, Disalvo.F.J, Mahajan.S, Adv.Phys.24, 117(1975).

(2) Comes.R, Lambert.M, Launois.H, Zeller.H.R, Phys.Rev.B 8, 571(1973).

(3) Iizumi.M, Axe.J.D, Sherane.G, Shimaoka.K, Phys.Rev.B 15, 4392 (1977).

(4) Peierls.R.E, Quantum theory of solids Oxford press, P 108 (1955).

(5) Frohlich.H, Proc.Royal.soc.A 223, 296 (1954).

(6) Overhauser.A.W, Phys.rev. 167, 691 (1968).

(7) Wilson.J.A and Yoffe.A.D, Adv.Phys. 18, 193 (1969).

(8) Thompson.A.H, Phys.Rev.Lett. 34, 520 (1975).

(9) Barmatz.M, Testardi.L.R and F.J.Disalvo, Phys.Rev.B 12, 4367 (1975).

(10) Naito.M and Tanaka.S, Proc.of.the.Yamada.conf.IV Phys and chem of Layered Materials, Sendai, P 130 (1980).

(11) Suits.B.H and Chen.M.C, Phys Lett, V 79A, No 2,3, 224 (1982).

(12) Fleming R.M, Moncton.D.E, Mcwhan D.B and Disalvo.F.J, Phys.Rev.Lett. 45, 576 (1980).

(13) Moncton.D.E, Axe.J.D, Disalvo.F.J, Phys.Rev.B 5, 801 (1977).

(14) Bak.P, Mukamel.D, Villain.J and Wentowska.K, Phys.Rev.B 19, 1610 (1979).

(15) Fung.K.K, Mckernan.S, Steeds.J.W and Wilson.J.A, J.Phys. C 14, 5417 (1981).

(16) Chen.C.H, Gibson.J.M, Fleming.R.M, Phys.Rev.Lett. 47, 723 (1981).

(17) Walker.M.B and Jacobs.A.E, Phys.Rev.B 24, 6770 (1981).

(18) Littlewood.P.B and Rice.T.M, Phys.Rev.lett. 48, 27 (1981).

(19) Suits.B.H, Couterie.S and Slichter.C.P, Phys.Rev.B 23, 5142 (1981).

(20) Butz.T, Vasquez.A and Lerf.A, J.Phys.C 12, 4505 (1979).

(21) Moceau.P, Ong.N.P, Partis.A.M, Meerschant.A and Rouxel.J, Phys.Rev.lett. 37, 602 (1976).

(22) Fleming.R.M, Moncton.D.E and Mcwhan.D.B, Phys.Rev.B 18, 5560 (1978).

(23) Disalvo.F.J and Fleming.R.M, Solid State Communications, V 35, 685 (1980).

(24) R.D.Barnard Thermoelectric measurements Taylor and Francis Ltd London, P 37 (1972).

(25) Macdonald.D.K.C, Pearson.W.B and Tempeleton.I.M, Proc.R.Soc.A 266, 161 (1962).

(26) Barnard.R.D, Thermoelectric measurements, Taylor and Francis Ltd London, P 144 (1972).

(27) Harper.J.H, Geballe.T.H and Disalvo.F.J, Phys.Rev. B 15, 2943 (1977).

(28) Barnard.R.D, Thermoelectric measurements, Taylor and Francis Ltd, P 139 (1972).

(29) Wilson.J.A, Phys.Rev.B 15, 5748 (1977).

(30) Barnard.R.D, Thermoelectric measurements Taylor and Francis Ltd, P 113 (1972).

(31) Frank J. Blatt, Peter A. Schroeder, Carl L. Foiles and Denis Greig, Thermoelectricpower of Metals Plenum press, New York, P 17 (1976).